

Altermagnetism and superconductivity in a multiorbital t - J model

Anjishnu Bose^{✉,*}, Samuel Vadnais,^{*} and Arun Paramekanti^{✉,†}

Department of Physics, University of Toronto, 60 St. George Street, Toronto, Ontario M5S 1A7, Canada



(Received 31 March 2024; revised 22 October 2024; accepted 24 October 2024; published 8 November 2024)

Motivated by exploring correlated multiorbital altermagnets ($A\ell$ Ms) we study minimal t - J models on the square-octagon lattice, which favors such a collinear magnetic order. While antiferromagnetic order breaks translational and time-reversal symmetries, the $A\ell$ M state (equivalently, a “ d -wave ferromagnet”) features multipolar order, which separately breaks time-reversal and crystal rotation symmetries but preserves their product leading to spin-split bands with zero net magnetization. We study the mean-field phase diagram of these multiorbital models as we vary doping and interactions, discovering two types of $A\ell$ M order: (i) itinerant weak-coupling $A\ell$ M metals driven by quasi-1D van Hove singularities, as well as (ii) strong $A\ell$ M order at half-filling. We also find regimes of superconductivity including uniform s -wave and d_{xy} -wave pairing states, incipient d_{xy} -wave pair density wave order, and uniform phases with coexisting singlet-triplet pairing and $A\ell$ M order. Our inhomogeneous mean-field theory approach reveals that the coexistence phases are unstable to phase separation, but longer-range interactions could lead to stripe order. Our results may be relevant to studies of doping and pressure on $A\ell$ M materials.

DOI: [10.1103/PhysRevB.110.205120](https://doi.org/10.1103/PhysRevB.110.205120)

I. INTRODUCTION

The one-band Hubbard and tJ models have been extensively investigated following the discovery of high-temperature cuprate superconductivity [1–4]. These models are thought to capture the physics of a wide variety of correlated superconductors, which descend from nearby states with Mott insulating antiferromagnetic order or other collinear spin density wave orders [3,5–8]. Indeed, fluctuating magnetism is thought to be the “pairing glue” responsible for unconventional superconductivity [9–12]. In this context it is interesting to explore the effect of doping on materials with more complex collinear magnetic orders such as the recently discovered altermagnet ($A\ell$ M) order [13,14]. Altermagnets are naturally multiorbital systems, which host magnetic order that is akin to a type of multipolar order [15]. $A\ell$ Ms preserve translational symmetry, unlike AFMs. While they break time-reversal and lattice rotation symmetries, they preserve the product of these two symmetries, which leads to zero net magnetization while still hosting spin-split bands [16–19]. This makes $A\ell$ Ms of potential interest for spintronic applications [20,21], and several candidate materials such as CrSb [22], Mn₅Si₃ [23], MnTe [24], κ -Cl [25], and many others have been experimentally explored. Recent studies have explored the Landau theory of altermagnets [26], their symmetry classification and their nodal excitations [27–29], and coupling of magnetism to phonons [26,30]. Electrons, which are proximity coupled to magnetic fluctuations in such altermagnets can potentially form p -wave triplet superconductors [31–34], while proximity coupling of $A\ell$ M to conventional superconducting states or

superconductivity induced by local pairing interactions could support pair density wave states and topological superconductivity [35–37] with edge or corner Majorana modes [37,38], and $A\ell$ M order can mediate unconventional Josephson effects [39], or diode effects [40]. In this context, it is interesting to explore possible superconductivity in doped or pressurized $A\ell$ M ordered materials.

A second important ingredient of superconductivity in many of the correlated quantum materials is that they exhibit multiple bands, at or near the Fermi level, which emerge from multiple atomic orbitals or multiple atoms in the unit cell. Such multiorbital models are important for a careful microscopic modeling of the CuO₂ layers in the cuprate superconductors [41–47], and play a more direct role in superconductors like Sr₂RuO₄ [48–51] and the more recently discovered iron-based [52] and nickel-based high-temperature superconductors [53–61]. Multiorbital models also leads to a more natural description of the rich variety of orders found generically in these systems including stripe and nematic orders [62–64]. It is thus interesting to ask if multiorbital systems can also more naturally host unusual superconductivity associated with nonzero-momentum pairing called “pair density wave order,” which have been found in numerical studies of simple phenomenological models [65–70].

Motivated by both the above sets of observations, our paper explores tJ models in a multiorbital system. We consider a square-octagon lattice model, which can support either AFM or $A\ell$ M order depending on the sign of certain exchange interactions; such a lattice, explored in previous theoretical studies [71–73], has been proposed to be relevant to certain transitional metal dichalcogenide and nitrogen group monolayers [74,75]. We study this lattice model as an illustrative model of how magnetic exchange interactions in an $A\ell$ M could potentially drive superconductivity. The

*These authors contributed equally to this work.

†arun.paramekanti@utoronto.ca

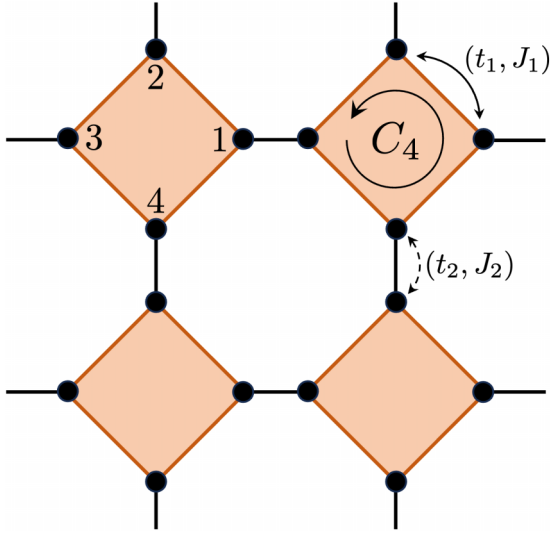


FIG. 1. Decorated square lattice model, also known as the square-octagon lattice, with four-site unit cell. The intracell hopping and spin exchange are denoted by (t_1, J_1) , and intercell hopping and spin exchange are denoted by (t_2, J_2) . We set $t_1 = 1$, $t_2 = t_1/2$, and $J_2/J_1 = -J/4$. We vary the electron filling \bar{n} and interaction J_1/t , keeping $J_1 > 0$.

simplest AℓM order, which we will consider in this paper may be termed a *d*-wave ferromagnet. Starting with this model, we study the effect of doping and interactions in such *tJ* models using mean-field theory, exploring both uniform symmetry broken states as well as possible spatially modulated orders. Our main result is that the resulting phase diagram contains a rich plethora of phases, which include metallic or insulating phases with strong AFM/AℓM order at half-filling, metallic phases with itinerant weak-coupling AℓM order or *d*-wave spin density wave states induced by quasi-one-dimensional van Hove singularities, as well as *s*-wave and *d*-wave paired superconductors. We also find regimes of incipient *d*-wave pair density wave states over a range of densities at weak coupling, which could potentially be stabilized with additional nonlocal interactions. In addition, we find states where AFM/AℓM order coexists with *d*-wave superconductivity leading to mixed singlet-triplet pairing, which, however, appear unstable to phase separation into droplets with Mott insulating AFM/AℓM order and droplets with *d*-wave superconductivity—these may form more organized structures (e.g., stripes) in the presence of longer-range interactions.

II. MULTIORBITAL MODEL

We consider a decorated square lattice model with four sites per unit cell as depicted in Fig. 1. The Hamiltonian we study is

$$H = - \sum_{\langle i,j \rangle, \sigma} t_{ij} (c_{i\sigma}^\dagger c_{j\sigma} + \text{H.c.}) + \sum_{\langle i,j \rangle} J_{ij} \mathbf{S}_i \cdot \mathbf{S}_j - \mu \sum_i n_{i\sigma}. \quad (1)$$

Here, the intracell and intercell nearest-neighbor hoppings are $t_{ij} = t_1$ and $t_{ij} = t_2$ respectively, and the corresponding

spin exchange couplings on those bonds are denoted by $J_{ij} = J_1$ and $J_{ij} = J_2$, respectively. We set $t_1 = 1$ to define the unit of energy, fix parameters $t_2/t_1 = 1/2$, consider different J_2/J_1 , and tune the electron filling $0 < \bar{n} < 1$ and interaction strength J_1/t_1 . $\bar{n} = 1$ corresponds to eight electrons per unit cell. While the $J_2 > 0$ arises naturally from a Hubbard model, the case $J_2 < 0$ can only arise from additional Hund's coupling physics with multiple on-site orbitals, so we view it here only as a convenient model Hamiltonian to capture AℓM order in this example.

We are not implementing strict Gutzwiller projection of the electrons in this study—we may view these *tJ* models as having renormalized hopping and interactions in the spirit of “renormalized mean-field theory” [4,76]. In this case, the filling-dependent renormalization of hopping and exchange couplings are given by $t \equiv g_t t_{\text{bare}}$ and $J \equiv g_J J_{\text{bare}}$, where $g_t = (1 - 2\bar{n})/(1 - \bar{n})$ and $g_J = 1/(1 - \bar{n})^2$. This results in the renormalized $J/t \equiv \lambda(\bar{n})(J/t)_{\text{bare}}$ where $\lambda(\bar{n}) = g_J/g_t$. The above result leads to

$$\lambda(\bar{n}) = \frac{1}{(1 - 2\bar{n})(1 - \bar{n})}. \quad (2)$$

Alternatively, we may simply view this *tJ* model as a toy model to explore magnetic and pairing instabilities driven by exchange interactions within unrestricted Hartree-Fock-Bogoliubov theory in the spirit of earlier study on the one-band model for cuprates [77].

This Hamiltonian has lattice symmetries including translation, a C_4 rotation around the center of the squares, inversion \mathcal{I} around the center of the squares and octagons, four mirror symmetries \mathcal{M} , and time-reversal \mathcal{T} . The symmetries of the Hamiltonian also include internal symmetries like $SU(2)$ spin rotation, and a particle-hole symmetry.

A. Orbital basis

In the absence of interactions, it is useful to solve the single unit cell in terms of “orbitals”. We label each site *i* in terms of unit-cell position **r** and basis $\ell = 1-4$. Using this, the orbitals correspond to

$$s_{\mathbf{r}\sigma} = \frac{1}{2}(c_{\mathbf{r}1\sigma} + c_{\mathbf{r}2\sigma} + c_{\mathbf{r}3\sigma} + c_{\mathbf{r}4\sigma}), \quad (3)$$

$$d_{\mathbf{r}\sigma} = \frac{1}{2}(c_{\mathbf{r}1\sigma} - c_{\mathbf{r}2\sigma} + c_{\mathbf{r}3\sigma} - c_{\mathbf{r}4\sigma}), \quad (4)$$

$$X_{\mathbf{r}\sigma} = \frac{1}{\sqrt{2}}(c_{\mathbf{r}1\sigma} - c_{\mathbf{r}3\sigma}), \quad (5)$$

$$Y_{\mathbf{r}\sigma} = \frac{1}{\sqrt{2}}(c_{\mathbf{r}2\sigma} - c_{\mathbf{r}4\sigma}), \quad (6)$$

which are respectively *s* orbital, *d* orbital, and a pair of degenerate *p* orbitals *X*, *Y*. The corresponding energies for a single unit cell are $\varepsilon_s = -2t_1$, $\varepsilon_X = \varepsilon_Y = 0$, $\varepsilon_d = +2t_1$. These orbitals will form corresponding bands, which for $t_2 \ll t_1$ are nonoverlapping. The resulting band structure is shown on the left side panel, in Fig. 2. In this case, with increasing filling, we go from filling the *s*-orbital band, to the *X*, *Y*-orbital bands, and eventually the *d*-orbital band, with gapped band insulators appearing in between when some of these bands are filled. This is also reflected in the density of states(DOS) shown on the right-hand side of Fig. 2, where 2D van Hove singularities

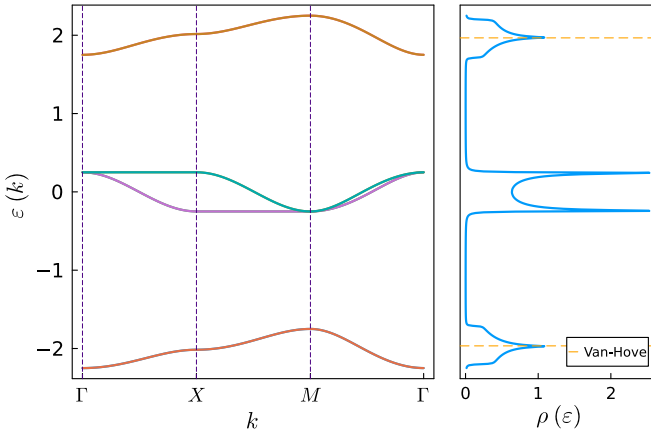


FIG. 2. (Left) Band structure of the multiorbital model studied, showing the s (low energy), X/Y (intermediate energy), and d (high energy) bands along high-symmetry path Γ - X - M . The gap between the bands $\sim 2t_1$, which is evident from the single unit-cell solution. (Right) Density of states (DOS) of the noninteracting multiorbital model. In addition to the s - X/Y and X/Y - d band gaps, the DOS shows a 2D van Hove singularity (vHS) in the s -band (d -band) at filling $n \sim 0.125$ ($n \sim 0.875$) as well as quasi-1D X/Y -band vHS at $n \sim 0.26, 0.74$.

(vHS) are present in the s and d bands, as well as quasi 1D vHS in the X/Y bands.

B. Fermi surfaces

We begin by exploring the Fermi surfaces of this square-octagon lattice model at various fillings, both in a symmetry-unbroken phase and in the presence of symmetry-breaking $A\ell M$ order. To study the impact of $A\ell M$ order, we incorporate a translationally invariant but basis-site-dependent Weiss magnetic field in the unit cell, which takes on value $+h$ for basis sites 1,3 and $-h$ for basis sites 2,4, which reflects the broken symmetry of the $A\ell M$, so

$$H_{A\ell M, \text{Weiss}} = h \sum_{\mathbf{r}\ell\alpha} (-1)^\ell c_{\mathbf{r}\ell\alpha}^\dagger \sigma_{\alpha\beta}^z c_{\mathbf{r}\ell\beta}. \quad (7)$$

The strength of this Weiss field will depend on the microscopic details such as exchange interactions and filling, which we will later explore within a self-consistent mean-field treatment of exchange interactions—for now, we simply choose a fixed value for h to illustrate the impact of $A\ell M$ order on the Fermi surfaces.

1. Low filling

The spin-degenerate Fermi surfaces of the full eight-band model (including spin) are shown in Fig. 3 (left) at a filling $\bar{n} = 0.2$. To understand this, we note that for fillings $\bar{n} < 0.25$, the partially occupied bands arise from the s orbitals as given in (3). This leads to an effective s -orbitals hopping Hamiltonian, which resembles a simple square lattice with nearest-neighbor hopping t_2 , with an effective Hamiltonian

$$H_s^{\text{eff}} = \sum_{\mathbf{k}} \varepsilon_{\mathbf{k}}^s s_{\mathbf{k}\sigma}^\dagger s_{\mathbf{k}\sigma}, \quad (8)$$

$$\varepsilon_{\mathbf{k}}^s = -2t_1 - \frac{t_2}{2} (\cos k_x + \cos k_y), \quad (9)$$

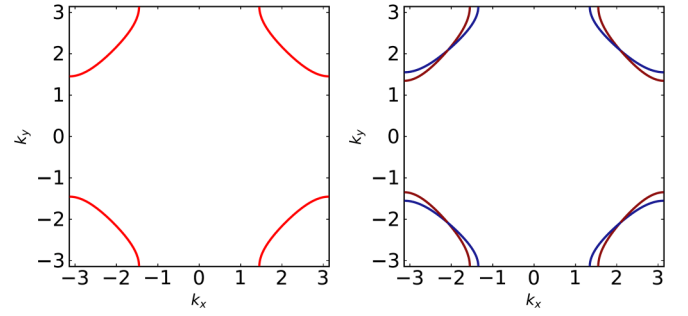


FIG. 3. Hole-like Fermi surfaces at $\bar{n} = 0.2$ filling where the s -orbital band, with dispersion minimum at the Γ point, is more than half-filled. (Left) In the absence of $A\ell M$ order, with spin degenerate FSs. (Right) Illustrative example of FSs if we incorporate $A\ell M$ order with parameters $t_1 = 1.0$, $t_2 = 0.5t_1$, $h = 0.5t_1$. The coloring of the bands indicates the spin polarization.

which has a minimum at the Brillouin zone (BZ) center $\Gamma = (0, 0)$ point. The filling of the s -band corresponds to $n_s^{\text{eff}} = 4\bar{n}$, so that the FS in Fig. 3 with $\bar{n} = 0.2$ corresponds to $n_s^{\text{eff}} = 0.8$.

Incorporating the basis-site-dependent $A\ell M$ Weiss field mentioned above leads to spin-splitting of the FSs as shown in Fig. 3 (right). It is straightforward to show that the basis-site-dependent Weiss fields on sites 1–4 vanishes if we simply project it to the s orbitals on each unit cell, so it has no impact on the FSs. Instead, the observed splitting of the s -band FS arises from perturbative mixing of the s -band with the Zeeman split X and Y orbital bands, which leads to an effective momentum-dependent Weiss field

$$H_s^{A\ell M} = -h \frac{t_2^2}{8t_1^2} \sum_{\mathbf{k}, \sigma=\pm} (\sin^2 k_x - \sin^2 k_y) \sigma s_{\mathbf{k}\sigma}^\dagger s_{\mathbf{k}\sigma}. \quad (10)$$

As an illustrative example, we set $h = 0.5t_1$. This leads to spin splitting at generic momenta on the Fermi surface except along four “ d -wave” nodes where the spin-up and spin-down Fermi surfaces cross when they intersect the $k_x = \pm k_y$ lines. This degeneracy is consistent with the fact that the altermagnet has x, y spatial mirror symmetries and preserves $\mathcal{T} \otimes \mathcal{C}_4$.

2. Intermediate filling

Figure 4 shows the FSs at intermediate filling, $\bar{n} = 1/2$ with and without an $A\ell M$ Weiss field respectively. For any filling $0.25 < \bar{n} < 0.75$, the bands can be effectively described in terms of an effective hopping Hamiltonian arising from X and Y orbitals hopping along their easy axis (x and y) respectively. This leads to a

$$H_p^{\text{eff}} = \sum_{\mathbf{k}} [\varepsilon_{\mathbf{k}}^X X_{\mathbf{k}\sigma}^\dagger X_{\mathbf{k}\sigma} + \varepsilon_{\mathbf{k}}^Y Y_{\mathbf{k}\sigma}^\dagger Y_{\mathbf{k}\sigma} + \varepsilon_{\mathbf{k}}^{XY} (X_{\mathbf{k}\sigma}^\dagger Y_{\mathbf{k}\sigma} + \text{H.c.})] \quad (11)$$

where $\varepsilon_{\mathbf{k}}^X = t_2 \cos k_x$, $\varepsilon_{\mathbf{k}}^Y = t_2 \cos k_y$, and an orbital mixing term with $\varepsilon_{\mathbf{k}}^{XY} = t' \sin k_x \sin k_y$. Direct projection does not lead to this orbital mixing term, but it is generated by perturbative processes, which virtually excite to the s, d orbitals so that $t' \approx t_2^2/2t_1$. Incorporating the $A\ell M$ Weiss field leads to

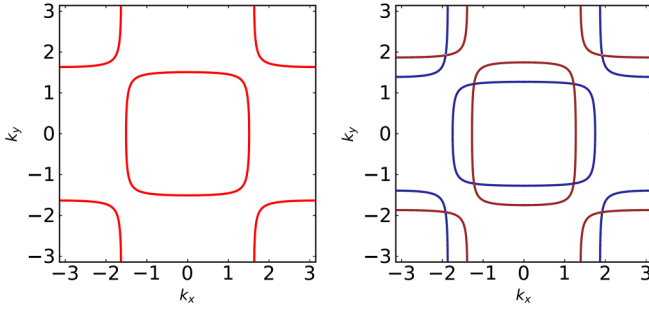


FIG. 4. Fermi surfaces at $\bar{n} = 0.5$ filling where the X, Y orbital bands are partially occupied. Left: In the absence of $A\ell M$ order, with spin degenerate FSs. Right: Illustrative example of FSs if we incorporate $A\ell M$ order with parameters $t_1 = 1.0$, $t_2 = 0.5t_1$, $h = 0.5t_1$. The coloring of the bands indicates the spin polarization.

the additional term

$$H_p^{A\ell M} = -h \sum_{\mathbf{k}\sigma=\pm} \sigma (X_{\mathbf{k}\sigma}^\dagger X_{\mathbf{k}\sigma} - Y_{\mathbf{k}\sigma}^\dagger Y_{\mathbf{k}\sigma}). \quad (12)$$

As an illustrative example, we again set $h = 0.5t_1$. The resulting FSs are shown in Fig. 4 without and with $A\ell M$ order. In the absence of $A\ell M$ order, we find two FS pockets, one centered at the $\Gamma = (0, 0)$ point and the other at (π, π) . With $A\ell M$ order, both FS pockets get spin split with eight band touching points along the $k_x = \pm k_y$ lines. We note that the $A\ell M$ spin splitting is much larger in this case with degenerate X/Y bands at the Fermi level, being $\sim h$, as opposed to the single band case discussed earlier where it is $(ht_2^2/t_1^2) \ll h$ because of indirect effects arising from perturbative coupling to the X/Y bands. This might suggest that multiorbital materials with multiple symmetry related bands at the Fermi level in the paramagnetic metal are likely to host stronger spin splitting once the system forms an $A\ell M$.

3. High filling

The simple model we have considered is particle-hole symmetric, invariant under $c_{\mathbf{r},i,\sigma} \rightarrow (-1)^{\mathbf{r}_i+\mathbf{r}_j} c_{\mathbf{r},i,\sigma}^\dagger$. This leads to a momentum dispersion for the high-energy d orbital derived bands at large filling \bar{n} , to be the same as the s -orbital band dispersion at low filling $1 - \bar{n}$ except for a shift in momentum by (π, π) . Figure 5 shows these FSs for $\bar{n} = 0.8$ without and with $A\ell M$ order.

C. Projected interacting Hamiltonians

We can simplify the full interacting Hamiltonians by projecting to specific orbitals at various fillings. For low filling, $0 < \bar{n} < 1/4$, we can project to the s orbital. At intermediate filling, $1/4 < \bar{n} < 3/4$, the physics is governed by the X, Y orbitals. Finally, at high fillings, $3/4 < \bar{n} < 1$, we project to d -orbital states. Since the Hamiltonian has particle-hole symmetry, the physics in the s orbital dominated regime at low filling $\bar{n} < 1/4$ is the same as the d -orbital regime at high filling $1 - \bar{n} < 1/4$. These simplified models will be useful for interpreting our full numerical mean-field results discussed in the following section. We note that if we use renormalized mean-field theory for the constrained tJ (crudely accounting

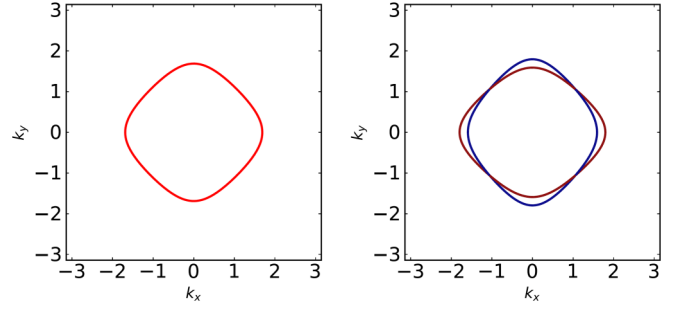


FIG. 5. Electron-like Fermi surfaces at $\bar{n} = 0.8$ filling where the d -orbital band is partially occupied. (Left) In the absence of $A\ell M$ order, with spin degenerate FSs. (Right) Illustrative example of FSs if we incorporate $A\ell M$ order with parameters $t_1 = 1.0$, $t_2 = 0.5t_1$, $h = 0.5t_1$. The coloring of the bands indicates the spin polarization.

for projecting out double occupancy via Gutzwiller factors), then the effective $(J/t)_{\text{eff}} = (J/t)_{\text{bare}}$.

1. Low/high filling

For $\bar{n} < 1/4$, we invert the above Eq. (3) and then project to the s orbital, which we can account for by setting $c_{\mathbf{r}\ell\sigma} \rightarrow s_{\mathbf{r}}/2$ for all sublattices $\ell = 1-4$. Using this, we find

$$H = -\frac{t_2}{4} \sum_{\langle \mathbf{r}, \mathbf{r}' \rangle, \sigma} (s_{\mathbf{r}\sigma}^\dagger s_{\mathbf{r}'\sigma} + \text{H.c.}) - \mu \sum_{\mathbf{r}\sigma} s_{\mathbf{r}\sigma}^\dagger s_{\mathbf{r}\sigma} - \frac{3J_1}{8} \sum_{\mathbf{r}} n_{\mathbf{r}\uparrow}^{(s)} n_{\mathbf{r}\downarrow}^{(s)} + \frac{J_2}{16} \sum_{\langle \mathbf{r}, \mathbf{r}' \rangle} \mathbf{S}_{\mathbf{r}} \cdot \mathbf{S}_{\mathbf{r}'} \quad (13)$$

where $n_{\mathbf{r}\sigma}^{(s)} = s_{\mathbf{r}\sigma}^\dagger s_{\mathbf{r}\sigma}$ and $\mathbf{S}_{\mathbf{r}}$ is the s -fermion spin operator. The intracell exchange interactions and intercell hopping thus lead to an effective square lattice *attractive* Hubbard model with $U_{\text{eff}}/t_{\text{eff}} = 3J_1/2t_2$, which will favor s -wave superconductivity as observed in our mean-field calculations. Weak ferromagnetic intersite exchange interaction J_2 is not expected to qualitatively modify the physics of this superconductor.

For high filling, $\bar{n} > 3/4$, the projected model looks identical because of a particle-hole symmetry. The only difference is that we should replace $s_{\mathbf{r}\sigma} \rightarrow d_{\mathbf{r}\sigma}$ in Eq. (13) for the fermion operators.

2. Intermediate filling

For $1/4 < \bar{n} < 3/4$, we can similarly project the full Hamiltonian to the X, Y orbitals, setting $(c_1, c_2, c_3, c_4) \rightarrow (X, Y, X, Y)/\sqrt{2}$, where we have suppressed site and spin labels for convenience. This leads to the effective Hamiltonian

$$H = \sum_{\mathbf{k}} [\varepsilon_{\mathbf{k}}^X X_{\mathbf{k}\sigma}^\dagger X_{\mathbf{k}\sigma} + \varepsilon_{\mathbf{k}}^Y Y_{\mathbf{k}\sigma}^\dagger Y_{\mathbf{k}\sigma} + \varepsilon_{\mathbf{k}}^{XY} (X_{\mathbf{k}\sigma}^\dagger Y_{\mathbf{k}\sigma} + \text{H.c.})] + J_1 \sum_{\mathbf{r}} \mathbf{S}_{\mathbf{r}}^X \cdot \mathbf{S}_{\mathbf{r}}^Y - \mu \sum_{\mathbf{r}} (n_{\mathbf{r}\sigma}^X + n_{\mathbf{r}\sigma}^Y) + \frac{J_2}{4} \sum_{\mathbf{r}} (\mathbf{S}_{\mathbf{r}}^X \cdot \mathbf{S}_{\mathbf{r}+\hat{x}}^X + \mathbf{S}_{\mathbf{r}}^Y \cdot \mathbf{S}_{\mathbf{r}+\hat{y}}^Y) \quad (14)$$

where $\varepsilon_{\mathbf{k}}^X = t_2 \cos k_x$ and $\varepsilon_{\mathbf{k}}^Y = t_2 \cos k_y$. The operators $\mathbf{S}_{\mathbf{r}}^X, \mathbf{S}_{\mathbf{r}}^Y$ denote the spin operators for X, Y orbitals respectively; similarly $n_{\mathbf{r}}^X, n_{\mathbf{r}}^Y$ denote number of electrons in X, Y

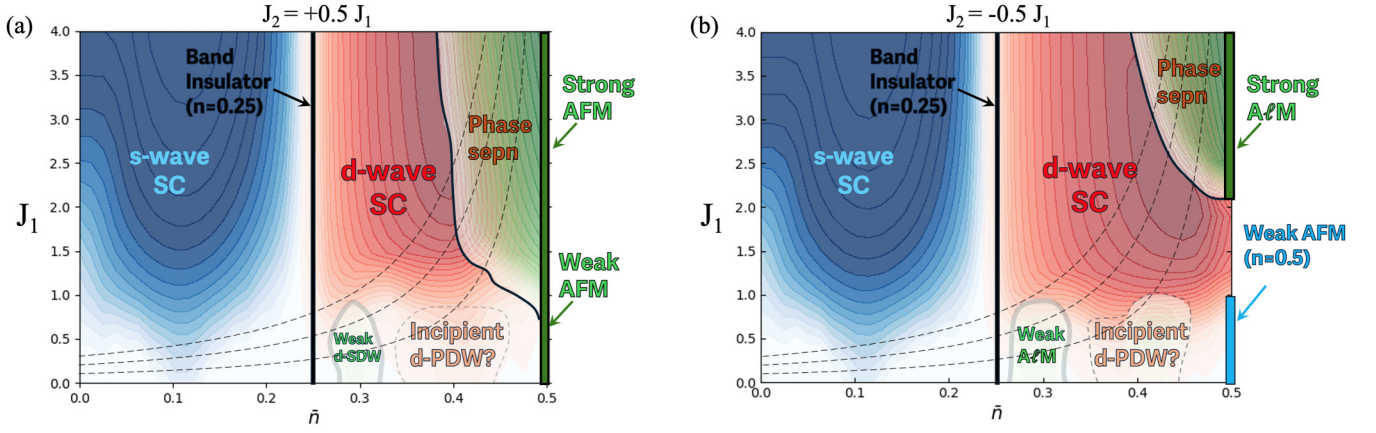


FIG. 6. Mean-field phase diagram of Hamiltonian in Eq. (1) with fixed $t_1 = 1$, $t_2 = 0.5t_1$, and intercell exchange coupling (a) $J_2 = +0.5J_1$ and (b) $J_2 = -0.5J_1$. Dashed lines indicate the renormalized exchange $\lambda(n)J_1$, with $\lambda(n)$ defined in Eq. (2), for $J_1 = 0.1, 0.2, 0.3$, which is applicable if this model is viewed as a renormalized mean-field tJ model of Gutzwiller projected electrons. In both models, $J_2 > 0$ and $J_2 < 0$ we find regimes of s -wave and d -wave superconductors with color contours indicating qualitative variation of the pair order parameter. Over a range of densities, the quasi-1D van Hove singularity leads to weak uniform AFM order for $J_2 < 0$, and a modulated d -spin density wave (d -SDW) order with AFM-type order within the unit cell for $J_2 > 0$. In addition, we find a window at weak coupling labeled “incipient d -PDW” where small system size calculations seem to favor (π, π) PDW with d -wave order over uniform d -wave SC, but the PDW order decreases with increasing system size (so the uniform d -SC wins at large system sizes). At half-filling and strong coupling, we find insulators with strong magnetic orders of AFM ($J_2 > 0$) or AFM ($J_2 < 0$) type. The region marked “Phase sepn” shows phase separation between d -wave SC and the insulating AFM or AFM order. The magnetization and pairing patterns for these phases are shown in Fig. 7, while the nature of phase separation is shown in Fig. 9.

orbitals, respectively. The effective model thus is a two-orbital model with *effective AFM Hund’s coupling* set by the exchange J_1 , and a much weaker intersite same-orbital exchange coupling $J_2/4$.

III. MEAN-FIELD PHASE DIAGRAM

We solve the t - J model Hamiltonian system in mean-field theory. We do this in real space by allowing for all possible mean-field channels: inhomogeneous hopping (including spin-dependent hopping), pairing (both singlet and triplet), and on-site densities, and magnetizations. The mean-field Hamiltonian, on any (i, j) bond, decomposed into these three channels looks like the following (all spin indices are being summed over):

$$H_{ij}^{\text{MF}} = (H_{\text{hop}} + H_{\text{loc}} + H_{\text{pair}}), \quad (15)$$

$$H_{\text{hop}} = c_{i\alpha}^\dagger \left(-t_{ij} \delta^{\alpha\beta} + \frac{J_{ij}}{4} \sigma_a^{\alpha\gamma} \sigma_a^{\delta\beta} \chi_{ji}^{\delta\gamma} \right) c_{j\beta} + \text{H.c.} \quad (16)$$

$$H_{\text{loc}} = c_{i\alpha}^\dagger \left(-\mu \delta^{\alpha\beta} + \frac{J_{ij}}{4} \sigma_a^{\alpha\beta} \sigma_a^{\gamma\delta} M_j^{\gamma\delta} \right) c_{i\beta} + i \leftrightarrow j \quad (17)$$

$$H_{\text{pair}} = c_{i\alpha}^\dagger \left(\frac{J_{ij}}{4} \sigma_a^{\alpha\gamma} \sigma_a^{\beta\delta} \Delta_{ji}^{\delta\gamma} \right) c_{j\beta}^\dagger + \text{H.c.} \quad (18)$$

where $\Delta_{ij}^{\alpha\beta} = \langle c_{i\alpha} c_{j\beta} \rangle$, $\chi_{ij}^{\alpha\beta} = \langle c_{i\alpha}^\dagger c_{j\beta} \rangle$, $M_i^{\alpha\beta} = \langle c_{i\alpha}^\dagger c_{i\beta} \rangle$. We solve for all channels self-consistently in real space, at each site and bond, allowing for a convergence tolerance of $\sim 10^{-3}$ for each parameter at a temperature $T/t_1 = 0.001$. We start with several different random initial conditions to maximize sampling of the full phase space and ensure that the target convergence is reached. The converged states are then compared to the uniform solution to confirm their stability. Figures 6(a)

and 6(b) show the phase diagrams obtained from the mean-field solution as we vary density \bar{n} and J_1 for fixed $J_2/J_1 = 0.5$ and $J_2/J_1 = -0.5$ respectively. We have also indicated dashed lines through the phase diagram, which corresponds to the variation of J_1 with density within a renormalized mean-field theory framework where the bare $J_1 \rightarrow \lambda(\bar{n})J_1$, with $\lambda(\bar{n})$ given by Eq. (2). Below we discuss some important aspects of these phase diagrams. We have also computed the mean-field phase diagram in momentum space allowing for 1×1 unit cell (four sites) and 2×2 unit cell (16 sites); this phase diagram is shown in Appendix B; we find that it is largely in agreement with Fig. 6 except in regimes, which show phase separation or incipient PDW order.

(i) *s*-wave SC. In both cases, the low density $\bar{n} < 0.25$ regime shows s -wave superconductivity. This is driven by the effective attractive Hubbard attraction induced by J_1 for the s orbital as seen from Eq. (13). Dominant singlet pairing mainly occurs on bonds between sites within the unit cell, with a weaker pairing on bonds connecting the diamond plaquettes. The largest pairing amplitude at any J_1 appears for densities $\bar{n} \approx 0.125$, which coincides with the 2D van Hove singularity in the density of states seen in Fig. 2. The structure of the pair amplitude on the unit cell is shown in Fig. 7(a), and the momentum-dependent spectral gap at the chemical potential is shown in Fig. 8(a).

(ii) *AFM order*. In both cases, we find a weak-coupling instability at half-filling ($\bar{n} = 0.5$) towards Néel AFM driven by nesting of the Fermi surfaces. We have confirmed this also within a random phase approximation (RPA) calculation discussed in the Appendix A 1. For the case $J_2 > 0$, this Stoner-type AFM order persists to strong coupling, much like in the one-band Hubbard model, leading to an AFM insulator. By contrast, for $J_2 < 0$, this Stoner AFM is lost as we move

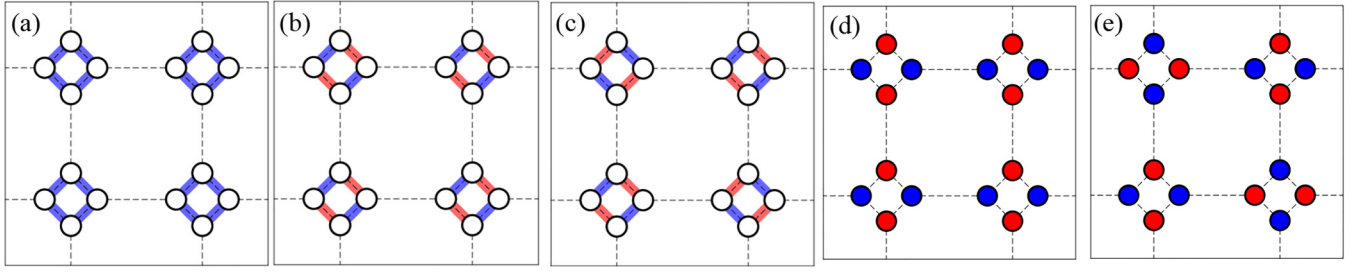


FIG. 7. Order parameter patterns found in a quadrupled unit cell mean-field theory calculations. (a) Uniform s -wave pairing with the same phase and strength of pairing on each intradiamond bond. (b) Uniform d -wave pairing with uniform strength but alternating phase of the pairing within the diamonds. (c) d -wave PDW with a d -wave pattern of pairing within the diamond, but now with a wave-vector of $\mathbf{M} = (\pi, \pi)$. (d) Altermagnet with red marking spin-up and blue marking spin-down on site. The altermagnet ordering wave-vector is, however, simply Γ . (e) AFM with similar ordering within the diamond as the altermagnet, but with a wave-vector of \mathbf{M} . The weak d -SDW is similar to AFM but has modulations at incommensurate wavevector driven by near nesting of Fermi surface segments.

towards strong coupling. Figure 7(e) depicts the magnetization in this AFM state.

(iii) *Strong A ℓ M order.* At half-filling, for $J_2 < 0$, going to strong coupling leads to A ℓ M order with a large ordered moment. This state remains metallic for A ℓ M Weiss fields $h < 2.0t_1$. At this critical value, the Fermi surface gaps out and the system transitions to an insulating A ℓ M phase. This insulating phase appears for $J_1 > 4.0t_1$, and is driven by local moments coupled through $J_1 > 0$ and $J_2 < 0$, as can be qualitatively understood through an effective spin-only model for the Mott insulator. Fig. 7(d) shows the structure of the magnetization in this A ℓ M state.

(iv) *Itinerant A ℓ M/SDW order.* Remarkably, for $J_2 < 0$, we find a second window of A ℓ M order at weak coupling, for densities $0.26 \lesssim \bar{n} \lesssim 0.3$, featuring a small ordered moment. This *itinerant* A ℓ M phase can be understood as being driven by the quasi-1D vHS seen in Fig. 2 corresponding to a low filling of the X, Y bands. In this regime, it is well known that the divergent DOS leads to a strongly enhanced ferromagnetic Stoner susceptibility for the quasi-one-dimensional X and Y bands. The weak A ℓ M phase then results from the effective AFM Hund's coupling seen in Eq. (14) between weakly ferromagnetic X and Y chains in the projected

two-orbital model. The itinerant A ℓ M state has the same symmetry as the strong-coupling A ℓ M, except for being metallic and featuring a highly reduced moment. Such an itinerant A ℓ M order would also be stabilized if we set $J_2 = 0$ but instead include intracluster or intercluster further neighbor repulsive interactions, so it could arise purely from an extended Hubbard model on the square-octagon lattice. We expect that this van Hove mechanism of A ℓ M order might also arise naturally in realistic models and materials with quasi-1D bands.

For $J_2 > 0$, we find a weak SDW ordering in the same density regime; however, the ordering wavevector is $\mathbf{Q} \approx \mathbf{M}/2$, with a d -type ordering within the unit cell (similar to the A ℓ M), so we label it as d -SDW. This ordering wavevector corresponds to the approximate nesting of the Fermi surface at these densities; this instability is bolstered by interactions (see Appendix A 1 for results from RPA calculation).

(v) *Uniform d -wave SC.* Both models, with weak $J_2 < 0$ and $J_2 > 0$, show large regimes of uniform singlet d -wave superconductivity for $0.25 < \bar{n} < 0.5$. This is primarily driven by the formation of singlet Cooper pairs on bonds with the unit-cell plaquettes, driven by AFM $J_1 > 0$, which can then delocalize across the lattice. In the projected model, this phase

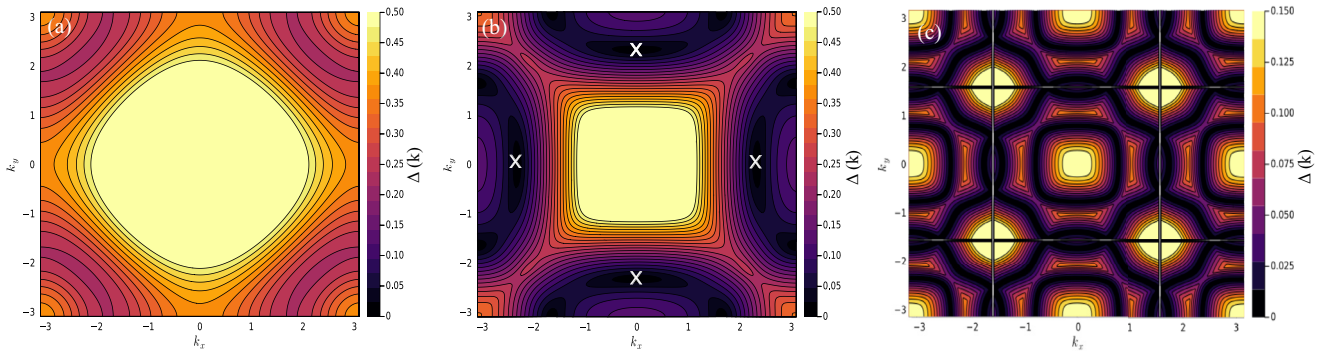


FIG. 8. Illustrative plot of the gap in the Bogoliubov quasiparticle spectrum at (a) $\bar{n} = 0.2$ with s -wave pairing strength $0.1t_1$; this refers to the SC pairing Weiss field in the BdG Hamiltonian. This value is realized around $J_1 \approx 1.5t_1$ in the self-consistent BdG mean-field theory, and it leads to a fully gapped spectrum. (b) $\bar{n} = 0.4$ also with d -wave pairing strength $0.1t_1$, which shows Dirac nodes (marked with crosses “x”) along the $\Gamma \rightarrow X$, and $\Gamma \rightarrow Y$ paths in the Brillouin zone. (c) The corresponding case when a (π, π) d -wave pairing with pairing strength $0.1t_1$ (this is exaggerated as compared to the mean-field results for illustrative purposes) is considered instead shows a gapless surface of quasiparticle excitations; for comparison with (b) we have plotted the spectrum in the original Brillouin zone.

can be simply viewed as the local AFM Hund's coupling leading to a nonzero on-site order parameter $\langle X^\dagger Y^\dagger \rangle$. Since C_4 rotation leads to $X \rightarrow Y$ and $Y \rightarrow -X$, this local order parameter changes sign in accordance with d -wave symmetry; more precisely, this is a SC with a d_{xy} order parameter. In several instances, we have found that real space solutions of the mean-field equations starting from random initial conditions result in d -wave droplets, which are not fully phase locked across the lattice, suggestive of a not-very-strong superfluid stiffness; in future work, we will address the superfluid stiffness in these regimes. However, in all these cases, we have checked that the uniform d -wave solution has a slightly lower energy than these phase-random d -wave droplet solutions. Figs. 7(b) and 8(b) show the pair amplitude in real space, and the momentum-dependent spectral gap at the chemical potential.

(vi) *d -wave PDW order.* Interestingly, for $J_1 \lesssim 1.0$ and for $0.38 \lesssim n \lesssim 0.48$, we find regimes of (π, π) d -wave PDW order in our inhomogeneous mean-field theory on system sizes upto 6×6 unit cells. In this d -PDW, electrons form singlet d -wave pairs within the unit cell but the pairing amplitude changes sign in the adjacent unit cell. Figure 7(c) shows the structure of the pair amplitude on the unit cell, and Fig. 8(c) shows the resulting momentum-dependent spectral gap in the full Brillouin zone. The RPA pairing susceptibility in the normal state shows significant peaks at $(0,0)$ and (π, π) (see Appendix A2); however, the most divergent low-temperature susceptibility is at $(0,0)$, suggesting that this finite size d -wave PDW order should disappear with increasing system size as we have confirmed using momentum space mean-field theory. However, the fact that the PDW state is favored on small system sizes suggests that slightly tuning the interactions, perhaps by including further neighbor interactions could favor this as the true ground state, as suggested in recent work on other models [70].

(vii) *Coexistence/phase separation.* Finally, in the strong coupling regime and for small doping away from half-filling, we find a regime where superconductivity and AFM or $A\ell M$ coexist in uniform mean-field theory as can be seen from the momentum space phase diagram in Appendix B. In this coexistence phase, the $A\ell M$ order mixes the real space singlet d -wave and triplet s -wave pairing with $S_z = 0$ on the diamond unit cell, which is allowed by the presence of multiple orbitals. Based on the symmetry analysis in Appendix C of possible pairing states, and given the proximity of the coexistence phase to the uniform d -wave singlet phase, we find that the superconductor coexisting with the $A\ell M$ phase is a superposition of d -wave singlet with s -wave triplet within the unit cell. These two states mix because C_4 and \mathcal{T} are broken by the $A\ell M$, but $C_4 \otimes \mathcal{T}$ is preserved under which both these pairing states are odd as shown in Table I. Allowing for a spatially inhomogeneous state, these coexisting orders phase separate, with the magnetically ordered regimes having density $\bar{n} \approx 0.5$ and forming $A\ell M$ droplets while the lower density regimes have d -wave pairing. In this regime, a uniform ansatz favors coexistence of AFM/ $A\ell M$ order with superconductivity. This coexistence leads to mixed singlet-triplet pairing within the unit cell; such $A\ell M$ -induced triplet pairing has been explored in recent work discussing $A\ell M$ fluctuation-induced pairing [31–34]. Incorporating longer-range repulsion between doped

charges could lead to organization of these phase separated regions into stripe or checkerboard states as has also been found in models for the cuprate superconductors. Figure 9 shows the typical structure of the density, magnetization, and pairing amplitude in such a phase separated state.

IV. SUMMARY AND DISCUSSION

Motivated by exploring t - J models, which capture $A\ell M$ order and to study the possible effects of doping and pressure-tuning of bandwidth, we have discussed a mean-field theory of a minimal model on the square-octagon lattice. This is shown to have a phase diagram, which includes multiple types of $A\ell M$ order—a strongly ordered $A\ell M$ phase with large moment at strong coupling and half-filling, and a weakly ordered itinerant $A\ell M$ metallic phase driven by quasi-1D van Hove singularities. The latter suggests a possible alternative design route to realizing weak itinerant $A\ell M$ order in materials. In addition, our phase diagram features multiple types of superconducting orders including s -wave, d -wave, and possible d -wave PDW order. For $J_2 > 0$ coupling between unit cells, this leads to locally $A\ell M$ -type configuration, which is modulated at an incommensurate wavevector Q , which we have dubbed d -SDW. We discussed the spatial structure of the various broken symmetry states and presented aspects of the spectral gap features in these phases. We are currently exploring if incorporating additional interactions in this model could stabilize stable PDW order. It would be interesting to also explore if such a rich set of orders are generic in other $A\ell M$ models with orbital and spin order, which have been explored in recent work [78,79], which would provide further motivation for experimentalists to search for superconductivity in doped or pressurized $A\ell M$ materials. Finally, incorporating weak spin-orbit coupling effects in these t - J models might be a route to interesting topological superconducting phases and would be a useful direction for future research.

ACKNOWLEDGMENTS

This research was funded by the Natural Sciences and Engineering Research Council (NSERC) of Canada. S.V. was supported by a scholarship from the Fonds de recherche du Québec - Nature et Technologies (FRQNT, Quebec). Numerical computations were performed on the Niagara supercomputer at the SciNet HPC Consortium and the Digital Research Alliance of Canada. The Julia codes for mean-field simulations and tight-binding analysis are available online at [80] and [81]. The bare susceptibility results were done in Julia as well as using TRIQS [82]

APPENDIX A: SUSCEPTIBILITIES

To get an idea of possible instabilities, one can calculate the susceptibility of these multiorbital or multi-sublattice model towards them. The formulation is a bit more involved but essentially the same as the simple single-band case. Furthermore, to leading order, one can also look at the effects of the interaction under RPA type approximation. To begin by looking at bare susceptibilities, let us define the generalized

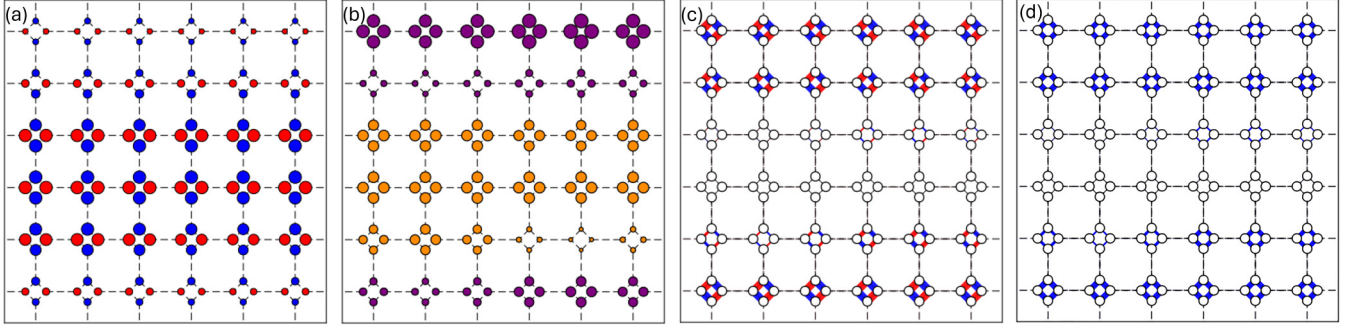


FIG. 9. Example of converged real space mean-field solution at $\bar{n} = 0.46$, $J_2 = -0.5J_1$, and $J_1 = 3.6$, showing phase separated state. (a) Inhomogeneous magnetic order of $A\ell M$ type with strong and weak $A\ell M$ regions. The weak $A\ell M$ order is induced by proximity to the strong $A\ell M$ region. Blue marks an on-site spin-up while red marks spin-down. (b) Density modulations, which track the $A\ell M$ modulations with strong $A\ell M$ order corresponding to density $\bar{n} \approx 0.5$ and weak $A\ell M$ regions having density $\bar{n} < 0.46$. Orange marks density higher than the mean filling while purple denotes the opposite. (c) Spatially inhomogeneous singlet pairing, and (d) spatially inhomogeneous triplet pairing. The mixture of d -wave singlet and s -wave triplet pairing in regions of low $A\ell M$ order is also driven by proximity to the $A\ell M$ domain, similar in spirit to the work by Brekke, *et al.* [31]. Blue and red denote opposite phases in the pairing, which give it the d -wave nature. Appendix C presents an analysis of the different pairing phases observed in the phase diagram.

order parameter (OP) fields corresponding to our orderings as follows:

(i) *Magnetic order.* Define the local magnetization OP fields as $M_{\mathbf{r},i}^a(\tau) = (1/2)c_{\mathbf{r},i,\alpha}^\dagger(\tau)\sigma_{\alpha\beta}^a c_{\mathbf{r},i,\beta}(\tau)$, where \mathbf{r} refers to the unit-cell position, i refers to every degree of freedom other than spin (such as sublattice or orbital), $a = x, y, z$ refers to the spin-ordering direction, and α, β refers to the fermion spin. In momentum space the corresponding vertex looks like

$$M_{\mathbf{Q},i}^a(i\Omega) = \sigma_{\alpha\beta}^a \int \frac{d^2k}{(2\pi)^2} \int \frac{d\omega}{(2\pi)} c_{\mathbf{Q}+\mathbf{k},i,\alpha}^\dagger(i\Omega + i\omega) c_{\mathbf{k},i,\beta}(i\omega), \quad (\text{A1})$$

where \mathbf{Q} is the exchange momentum and Ω is the exchange energy.

(ii) *Pairing order.* Now pairing is more complicated since one can have nonlocal pairing as well. To that end, a generalized pairing OP field will look like $\Delta_{\mathbf{r}+\delta/2}^{a,ij}(\tau) = (1/2)c_{\mathbf{r},i,\alpha}^\dagger(\tau)\sigma_{\alpha\beta}^a c_{\mathbf{r}+\delta,j,\beta}^\dagger(\tau)$ corresponding to a non-local pairing when $\delta \neq 0$. Such OP fields generically live on the bonds of the lattice as opposed to the magnetic ordering field living on-site. Again, in Fourier space, the vertex (which is now momentum dependent) looks like

$$\Delta_{\mathbf{Q},ij}^a(\delta; i\Omega) = \sigma_{\alpha\beta}^a \int \frac{d^2k}{(2\pi)^2} \int \frac{d\omega}{(2\pi)} c_{-\mathbf{k}+\mathbf{Q}/2,i,\alpha}^\dagger \times (-i\omega + i\Omega/2) c_{\mathbf{k}+\mathbf{Q}/2,j,\beta}^\dagger(i\omega + i\Omega/2) e^{i\delta \cdot \mathbf{k}}, \quad (\text{A2})$$

where \mathbf{Q} is the center of mass momentum and Ω is the center of mass energy.

Using these OP fields, we can calculate the bare susceptibility of the model as shown in the subsequent sections. To get ordering tendencies of the model, we have to diagonalize the zero-energy response matrix at all momenta. The eigenvector

with the largest eigenvalue corresponds to possible orderings with the ordering vector being the momentum at which this maximum eigenvalue occurs. One can repeat this exercise after performing RPA, which can affect possible orderings in the model as interaction strength is slowly increased. Encountering a diverging eigenvalue of the response corresponds to a phase transition into a symmetry broken state, which should match qualitatively with mean-field results. Alternatively, one can also tune the temperature at strong-coupling regime to extract information about phases beyond the first instability encountered at zero temperature when tuning the interaction.

1. Magnetic channel

The bare susceptibility, $\chi_{0,ij}^{ab}(\mathbf{Q}, i\Omega) = \langle M_{\mathbf{Q},i}^a(i\Omega) M_{\mathbf{Q},j}^{b,\dagger}(i\Omega) \rangle$ is equivalent to the usual spin-response function. Diagrammatically, it corresponds to a generalized bubble diagram. For spin-rotation symmetric systems, the connected piece of the diagram looks like

$$\chi_{0,ij}^{ab}(\mathbf{Q}, i\Omega) = -\frac{\delta^{ab}}{4} \int \frac{d^2k}{(2\pi)^2} \times \int \frac{d\omega}{(2\pi)} G_{ij}(\mathbf{Q} + \mathbf{k}, i\Omega + i\omega) G_{ji}(\mathbf{k}, i\omega), \quad (\text{A3})$$

where $G_{ij}^{\alpha\beta}(\mathbf{k}, i\omega) = \delta^{\alpha\beta} G_{ij}(\mathbf{k}, i\omega) = \langle c_{i,\alpha}(\mathbf{k}, i\omega) c_{j,\beta}^\dagger(\mathbf{k}, i\omega) \rangle$ are the bare Green's functions calculated in mean-field theory. In terms of the quasiparticle dispersion $\epsilon_n(\mathbf{k})$ and their corresponding wavefunctions $U_{ij}(\mathbf{k})$, these Green's functions can be expressed as

$$G_{ij}(\mathbf{k}, i\omega) = \sum_n U_{in}(\mathbf{k}) \frac{1}{i\omega - \epsilon_n(\mathbf{k}) + \mu} U_{nj}^\dagger(\mathbf{k}). \quad (\text{A4})$$

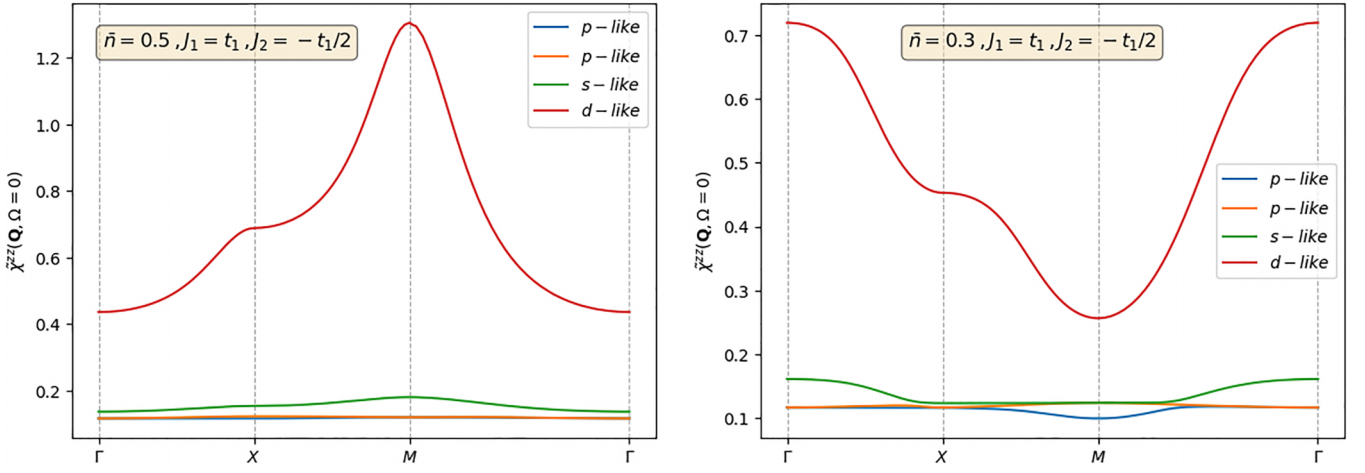


FIG. 10. The magnetic susceptibilities at zero-energy at a fixed low temperature of $T = 0.1t_1$ after performing RPA at $J_1 = t_1, J_2 = -0.5t_1$, plotted along a high-symmetry path in the Brillouin zone, at two different fillings. The labels are the same as in Fig. 12 (a) At half-filling, $\bar{n} = 0.5$, the ordering at $Q = M$ with a d -like eigenvector corresponding to the usual AFM ordering. (b) At some generic filling, $\bar{n} = 0.3$, the RPA susceptibility is peaked at $Q = \Gamma$, again with the d -type eigenvector. This corresponds to a $A\ell M$ type ordering.

Substituting this expression back into (A3), performing the Matsubara sum by hand, and analytically continuing the resulting expression $i\Omega \rightarrow \Omega + i\eta$, we get

$$\chi_{0,ij}^{ab}(\mathbf{Q}, \Omega) = \frac{\delta^{ab}}{4} \sum_{n,m} \int \frac{d^2k}{(2\pi)^2} U_{jn}(\mathbf{Q} + \mathbf{k}) U_{ni}^\dagger(\mathbf{Q} + \mathbf{k}) U_{im}(\mathbf{k}) U_{mj}^\dagger(\mathbf{k}) \frac{n_F(\epsilon_n(\mathbf{Q} + \mathbf{k}) - \mu) - n_F(\epsilon_m(\mathbf{k}) - \mu)}{\Omega + i\eta - (\epsilon_n(\mathbf{k} + \mathbf{Q}) - \epsilon_m(\mathbf{k}))}, \quad (\text{A5})$$

where n_F is the Fermi distribution function.

To perform RPA, let us focus on analyzing Heisenberg type interactions and decompose it in terms of the magnetic OP fields. We have a generalized Heisenberg type interaction on a lattice as

$$\mathcal{H}_{\text{int}} = \frac{1}{4} \sum_{\delta} \sum_{\mathbf{r}, \tau} J_{ij}(\delta) c_{\mathbf{r},i,\alpha}^\dagger(\tau) \sigma_{\alpha\beta}^a c_{\mathbf{r},i,\beta}(\tau) c_{\mathbf{r}+\delta,j,\mu}^\dagger(\tau) \sigma_{\mu\nu}^a c_{\mathbf{r}+\delta,j,\nu}(\tau). \quad (\text{A6})$$

Using the definition of the magnetic OP fields, we immediately see that

$$\mathcal{H}_{\text{int}} = \sum_{\delta} \sum_{\mathbf{r}, \tau} J_{ij}(\delta) M_{\mathbf{r},i}^a(\tau) M_{\mathbf{r}+\delta,j}^{a,\dagger}(\tau) = \sum_{\mathbf{Q}, \Omega} M_{\mathbf{Q},i}^a(\Omega) \left[\delta^{ab} \sum_{\delta} J_{ij}(\delta) e^{-i\mathbf{Q} \cdot \delta} \right] M_{\mathbf{Q},j}^{b,\dagger}(\Omega). \quad (\text{A7})$$

Hence, under RPA, the susceptibility will have the form

$$\chi_{ij}^{ab}(\mathbf{Q}, \Omega) = [(\mathbb{1} - \chi_0(\mathbf{Q}, \Omega) \cdot \tilde{J}(\mathbf{Q}))^{-1} \cdot \chi_0(\mathbf{Q}, \Omega)]_{ij}^{ab}, \quad (\text{A8})$$

where the effective interaction matrix is $\tilde{J}_{ij}^{ab}(\mathbf{Q}) = \delta^{ab} \sum_{\delta} J_{ij}(\delta) e^{-i\mathbf{Q} \cdot \delta}$, and \cdot denotes matrix multiplication in the spin-direction index a and sublattice/orbital index i .

For our model, with $J_2/J_1 < 0$ shown in Fig. 10, we find that at exactly half-filling $\bar{n} = 0.5$, there is an instability toward AFM order, which can be seen by the response peaking near the $Q = M = (\pi, \pi)$ point in the Brillouin zone. However, at every other generic filling, the system prefers $A\ell M$ ordering, peaking at the Γ point. In contrast, for $J_2/J_1 > 0$ as shown in Fig. 11, the instability toward AFM at half-filling remains, but at lower fillings near the van Hove singularities, the instability now occurs with $Q = M/2$. This behavior arises from Fermi-surface nesting around that filling, as can be seen even in the bare susceptibilities in Fig. 12.

2. Pairing channel

Let us look at the bare pairing susceptibility by repeating the steps as in the magnetic case (with a lot more indices to keep track of!). We want to calculate $\Gamma_{0,ijkl}^{ab}(\delta_1, \delta_2; \mathbf{Q}, i\Omega) = \langle \Delta_{\mathbf{Q},ij}^a(\delta_1; i\Omega) \Delta_{\mathbf{Q},kl}^{b,\dagger}(\delta_2, i\Omega) \rangle$. Working this bubble out in all its gory details gives us

$$\Gamma_{0,ijkl}^{ab}(\delta_1, \delta_2; \mathbf{Q}, i\Omega) = \frac{1}{4} \sigma_{\alpha\beta}^a \sigma_{\mu\nu}^b \int \frac{d^2k}{(2\pi)^2} \int \frac{d\omega}{(2\pi)} \left\{ e^{i\mathbf{k} \cdot (\delta_1 - \delta_2)} G_{ik}^{\alpha\delta}(-\mathbf{k} + \mathbf{Q}/2, -i\omega + i\Omega/2) G_{jl}^{\beta\gamma}(\mathbf{k} + \mathbf{Q}/2, i\omega + i\Omega/2) \right. \\ \left. - e^{i\mathbf{k} \cdot (\delta_1 + \delta_2)} G_{il}^{\alpha\mu}(-\mathbf{k} + \mathbf{Q}/2, -i\omega + i\Omega/2) G_{jk}^{\beta\nu}(\mathbf{k} + \mathbf{Q}/2, i\omega + i\Omega/2) \right\}. \quad (\text{A9})$$

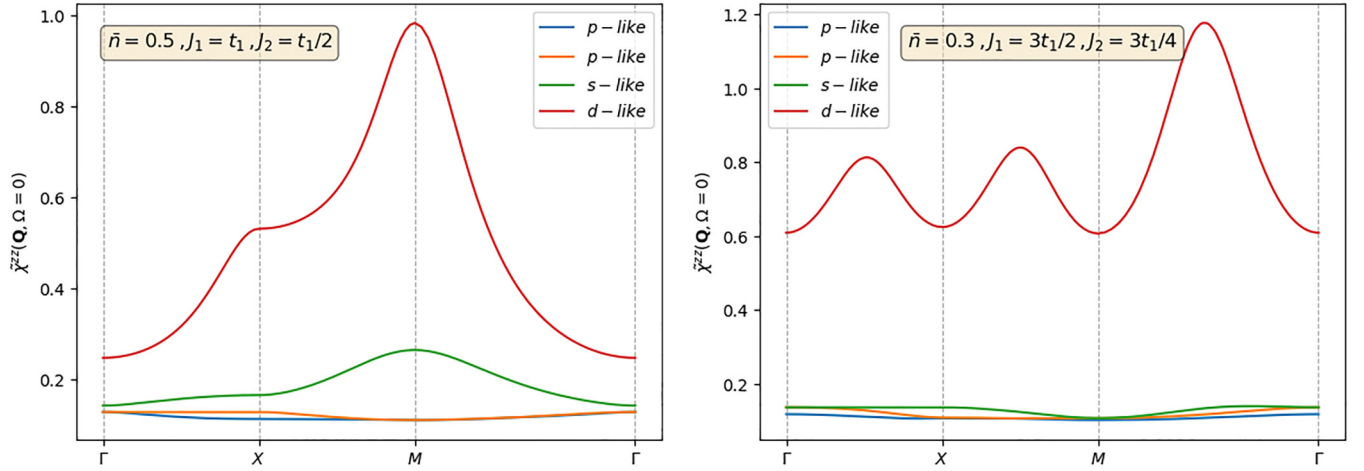


FIG. 11. The magnetic susceptibilities with $J_2/J_1 > 0$ at zero-energy at a fixed low temperature of $T = 0.1t_1$ after performing RPA, plotted along a high-symmetry path in the Brillouin zone, at two different fillings. The labels are the same as in Fig. 12 (a) At half-filling, $\bar{n} = 0.5$, the ordering at $Q = M$ with a d -like eigenvector corresponding to the usual AFM ordering. (b) At $\bar{n} = 0.3$ close to the van Hove singularities, the ordering is at $QM/2$ with a d -type eigenvector.

We can simplify the above expression when we use spin-rotation symmetry, which tells us that the pairing response can be categorized into singlet and triplet pairings. Defining a shorthand for one of the two contributions to the integral as

$$\mathcal{I}_{ijkl}(\delta; \mathbf{Q}, i\Omega) \equiv \int \frac{d^2k}{(2\pi)^2} \int \frac{d\omega}{(2\pi)} e^{i\mathbf{k} \cdot \delta} G_{ik}(-\mathbf{k} + \mathbf{Q}/2, -i\omega + i\Omega/2) G_{jl}(\mathbf{k} + \mathbf{Q}/2, i\omega + i\Omega/2), \quad (\text{A10})$$

we get that

$$\Gamma_{0,ijkl}^{ab}(\delta_1, \delta_2; \mathbf{Q}, i\Omega) = \begin{cases} \frac{1}{2}\mathcal{I}_{ijkl}(\delta_1 - \delta_2; \mathbf{Q}, i\Omega) - \frac{1}{2}\mathcal{I}_{ijlk}(\delta_1 + \delta_2; \mathbf{Q}, i\Omega), & a = b \in \{0, x, z\} : \text{triplet}, \\ \frac{1}{2}\mathcal{I}_{ijkl}(\delta_1 - \delta_2; \mathbf{Q}, i\Omega) + \frac{1}{2}\mathcal{I}_{ijlk}(\delta_1 + \delta_2; \mathbf{Q}, i\Omega), & a = b \in \{y\} : \text{singlet}, \\ 0, & a \neq b, \end{cases} \quad (\text{A11})$$

where $\sigma^0 = \mathbb{1}_{2 \times 2}$, the identity matrix. Focusing on \mathcal{I}_{ijkl} , we can repeat the steps as before, i.e., write everything using the band dispersion and wavefunctions, performing the Matsubara sum by hand, and analytically continuing the resultant expression. We

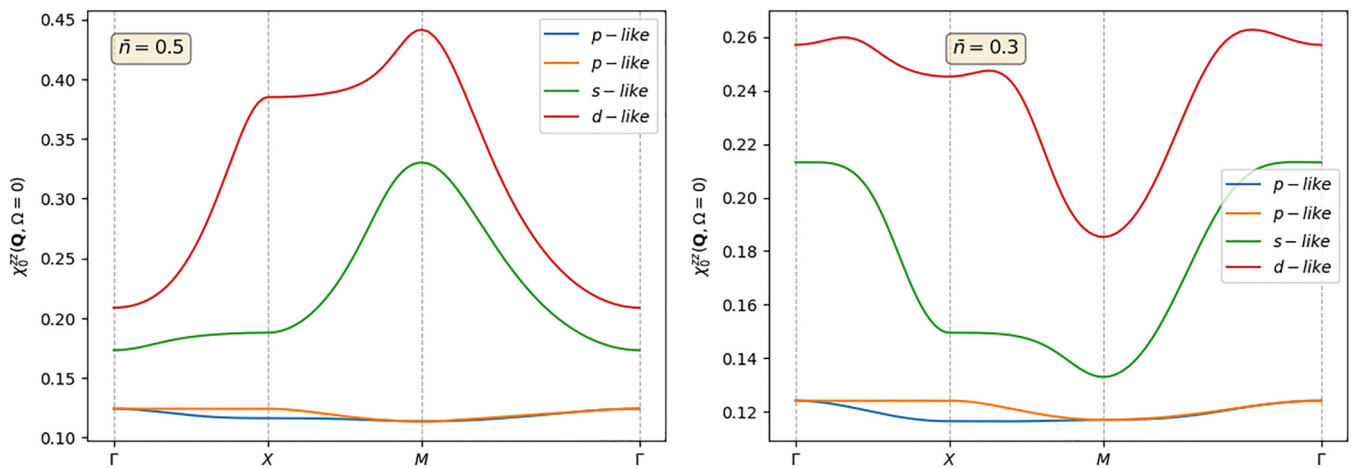


FIG. 12. The bare magnetic susceptibilities at zero energy, calculated at a fixed low temperature of $T = 0.1t_1$, are plotted along a high-symmetry path in the Brillouin zone, at two different fillings. The labels describe the eigenvectors of the susceptibility matrix such that s -like corresponds to all spins pointing parallel to each other in the unit cell, d -like corresponds to the spins alternating within the unit cell and so on. (a) At half-filling, $\bar{n} = 0.5$, where we find the ordering at $Q = M$ with a d -like eigenvector. This just corresponds to a usual AFM ordering. (b) At some generic filling, $\bar{n} = 0.3$, we find more complicated momentum-dependent behavior, which is peaked near $Q = \Gamma$, again with the d -type eigenvector.

end up with

$$\begin{aligned} \mathcal{I}_{ijkl}(\delta; \mathbf{Q}, \Omega) = & \sum_{n,m} \int \frac{d^2k}{(2\pi)^2} U_{kn}(-\mathbf{k} + \mathbf{Q}/2) U_{ni}^\dagger(-\mathbf{k} + \mathbf{Q}/2) U_{lm}(\mathbf{k} + \mathbf{Q}/2) U_{mj}^\dagger(\mathbf{k} + \mathbf{Q}/2) \\ & \times e^{i\mathbf{k} \cdot \delta} \cdot \left(\frac{n_F(\epsilon_n(-\mathbf{k} + \mathbf{Q}/2) - \mu) + n_F(\epsilon_m(\mathbf{k} + \mathbf{Q}/2) - \mu) - 1}{\Omega + i\eta - \epsilon_n(-\mathbf{k} + \mathbf{Q}/2) - \epsilon_m(\mathbf{k} + \mathbf{Q}/2) + 2\mu} \right). \end{aligned} \quad (\text{A12})$$

Now, for RPA in this channel, we will have to redo the decomposition of the interaction in terms of the pairing OP fields. We again start with (A6) and rearrange the terms as

$$\mathcal{H}_{int} = \frac{1}{4} \sigma_{\alpha\beta}^a \sigma_{\mu\nu}^a \sum_{\delta} \sum_{\mathbf{r}, \tau} J_{ij}(\delta) c_{\mathbf{r},i,\alpha}^\dagger(\tau) c_{\mathbf{r}+\delta,j,\mu}^\dagger(\tau) c_{\mathbf{r}+\delta,j,\nu}(\tau) c_{\mathbf{r},i,\beta}(\tau). \quad (\text{A13})$$

We see that we cannot simply substitute the form of our pairing OP fields since the spin indices are not as we want them in (A13). However, since the Heisenberg interaction is spin-rotation symmetric, we can again decompose it in terms of singlet and triplets. It turns out that the interaction then looks like

$$\begin{aligned} \mathcal{H}_{int} = & \frac{1}{4} \sum_{\delta} \sum_{\mathbf{r}, \tau} J_{ij}^{ab}(\delta) (c_{\mathbf{r},i,\alpha}^\dagger(\tau) \sigma_{\alpha\mu}^a c_{\mathbf{r}+\delta,j,\mu}^\dagger(\tau)) (c_{\mathbf{r}+\delta,j,\nu}(\tau) \sigma_{\nu\beta}^b c_{\mathbf{r},i,\beta}(\tau)) \\ = & \sum_{\delta} \sum_{\mathbf{r}, \tau} J_{ij}^{ab}(\delta) \Delta_{\mathbf{r}+\delta/2}^{a,ij}(\tau) \Delta_{\mathbf{r}+\delta/2}^{b,ij,\dagger}(\tau) \\ = & \sum_{\mathbf{Q}, \Omega} \Delta_{\mathbf{Q},ij}^a(\delta_1; \Omega) \left[\delta^{(ij),(kl)} \delta_{\delta_1, \delta_2} \sum_{\delta_1} J_{ij}^{ab}(\delta_1) \right] \Delta_{\mathbf{Q},kl}^{b,\dagger}(\delta_2; \Omega), \end{aligned} \quad (\text{A14})$$

where the interaction in the singlet-triplet pairing basis looks like

$$J_{ij}^{ab}(\delta) = \begin{cases} \frac{1}{2} J_{ij}(\delta), & a = b \in \{0, x, z\} : \text{triplet}, \\ -\frac{3}{2} J_{ij}(\delta), & a = b \in \{y\} : \text{singlet}, \\ 0, & a \neq b. \end{cases} \quad (\text{A15})$$

Note that the interaction is completely *momentum independent* in the center of mass basis, and diagonal in the pairing OP fields. The total RPA susceptibility takes on a similar form as (A8) as

$$\begin{aligned} \Gamma_{ijkl}^{ab}(\delta_1, \delta_2; \mathbf{Q}, i\Omega) \\ = [(\mathbb{1} - \Gamma_0(\mathbf{Q}, i\Omega) \cdot \mathcal{J}(\mathbf{Q}))^{-1} \cdot \Gamma_0(\mathbf{Q}, i\Omega)]_{ijkl}^{ab}(\delta_1, \delta_2), \end{aligned} \quad (\text{A16})$$

where $\mathcal{J}_{ij,kl}^{ab;\delta_1\delta_2}(\mathbf{Q}) = \delta^{(ij),(kl)} \delta_{\delta_1, \delta_2} \sum_{\delta} J_{ij}^{ab}(\delta)$, and \cdot now denotes matrix multiplication in all possible index degree of freedom including spin a , bond displacement δ , and pairing orbital/sublattices ij .

For simplicity, we chose to use the reduced two-orbital model instead of the full square-octagon model, and focus on singlet pairing susceptibility. The pairing OP fields we choose to work with are the ones, which can be generated through our interaction, namely $X - Y$ pairing on site $\Delta_{\mathbf{Q},XY}^y(\mathbf{0}; 0)$, $X - X$ pairing along the x bonds $\Delta_{\mathbf{Q},XX}^y(\hat{x}; 0)$, and $Y - Y$ pairing along the y bonds $\Delta_{\mathbf{Q},YY}^y(\hat{y}; 0)$. Note that since $\Delta_{\mathbf{Q},ij}^a(\delta; i\Omega) = \Delta_{\mathbf{Q},ji}^a(-\delta; i\Omega)$, we do not need to track $\delta = -\hat{x}$ and $\delta = -\hat{y}$ separately.

We find that the largest eigenvalue comes from the $X - Y$ pairing on-site as shown in Fig. 13. Upon RPA, above the critical temperature T_C , we find that the peak in the center of mass momentum is at the Gamma point $\mathbf{Q} = \Gamma$. However, we also note that there are secondary peaks at the \mathbf{M} points

as well, which explains the strong competition between a (π, π) PDW versus a simple d -wave pairing. In future works, one can imagine adding additional interactions, which will further enhance the peak at the \mathbf{M} points. Lastly, since its the J_1 interaction, which enhances these responses, changing the sign of J_2 from being ferromagnetic to antiferromagnetic shows minor changes in the susceptibility in the cases when $|J_2| \ll |J_1|$.

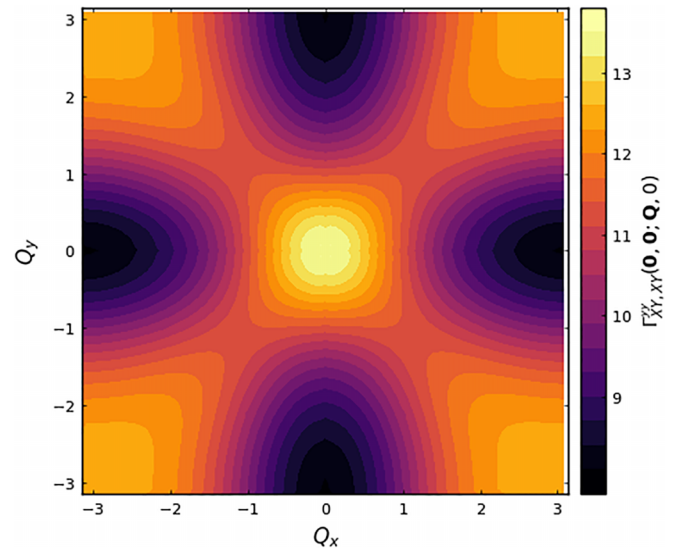


FIG. 13. The normal state RPA singlet pairing susceptibility with $t_1 = 1$, $t_2 = 0.5t_1$, $J_1 = 0.5t_1$, and $J_2 = -0.5J_1$ at $\Omega = 0$ and a fixed low temperature of $T = 0.13t_1$, plotted on the Brillouin zone for the reduced two-orbital model. The largest eigenvalue comes from the $X - Y$ singlet pairing on-site, which corresponds to a d -wave pairing in the original model.

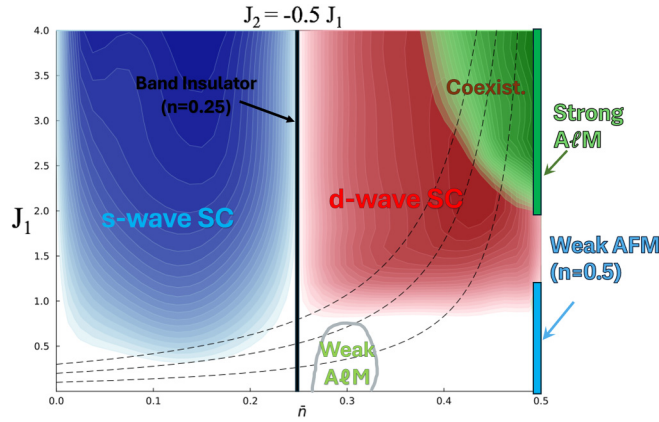


FIG. 14. Momentum space phase diagram for case $J_2 = -0.5J_1$, assuming 2×2 diamond enlarged unit cell. The dashed lines represent $(J_1/t)_{\text{eff}} = \frac{J_1}{1-2n(1-n)}$ for values of $J_1 = \{0.1, 0.2, 0.3\}$, where this effective exchange to hopping ratio arises from a renormalized mean-field theory of the tJ model as discussed in the main text.

APPENDIX B: MOMENTUM SPACE PHASE DIAGRAMS

In this Appendix, we perform a uniform mean-field theory assuming a quadrupled unit-cell, consistent with all uniform orders observed in our real space phase diagram. The resulting phase diagram is shown in Figure 14. The converged energies of these solutions were compared to the real space solution ones, and we found a quantitative match for all phases except for the one labelled 'phase separation' in the diagram.

APPENDIX C: SYMMETRY ANALYSIS OF PAIRING PHASES

In this Appendix, we will try to perform a symmetry analysis of various possible pairing phases seen in our phase diagram. To begin with, since we only encounter pairing within the squares of our square-octagon lattices, we will focus on such pairing states only. These *intradiamond* pairing states can be fully classified by their quantum numbers under real-space rotation, as well as spin-space rotation or time-reversal. The order parameters for these states can be represented succinctly in real space as [using the definition of pairing fields given in the above Eq. (A2)]

$$\Delta_l^a(\tau) = \sum_{\mathbf{r}} \left(\langle \Delta_{\mathbf{r}}^{a,12}(\tau) \rangle + e^{il\frac{\pi}{2}} \langle \Delta_{\mathbf{r}}^{a,23}(\tau) \rangle + e^{il2\frac{\pi}{2}} \langle \Delta_{\mathbf{r}}^{a,34}(\tau) \rangle + e^{il3\frac{\pi}{2}} \langle \Delta_{\mathbf{r}}^{a,41}(\tau) \rangle \right), \quad (\text{C1})$$

where $l \in \{0, \pm 1, 2\}$ represents the *angular momentum* of the pairing state (represented by s , p_{\pm} , and d respectively). Furthermore, the spin of the paired state is denoted by a ,

TABLE I. Quantum numbers of possible pairing states under symmetries of the Hamiltonian.

Pairing state	Order parameter	C_4	\mathcal{T}	\mathcal{I}	\mathcal{M}_x	\mathcal{M}_y
s -wave singlet	Δ_0^y	1	1	1	1	1
d -wave singlet	Δ_2^y	-1	1	1	-1	-1
s -wave triplet	Δ_0^x	1	-1	1	-1	-1
d -wave triplet	Δ_2^x	-1	-1	1	1	1

where $a = y$ represents singlets, while $a = x, z, 0$ represents triplets. The symmetry operations present in our Hamiltonian (1), by which we aim to classify the pairing states, include: rotation C_4 ; time-reversal \mathcal{T} ; inversion \mathcal{I} ; mirror along x , \mathcal{M}_x ; mirror along y , \mathcal{M}_y ; and spin-rotation symmetry \mathcal{R}_S . Let us start with the simplest of these: spin-rotation symmetry. We have already categorized the pairing states according to their total spin into singlets $S = 0$ and triplets $S = 1$. We can subsequently use S_z^{tot} quantum numbers to further classify the triplets themselves. Please note that even in the symmetry broken AℓM or AFM phases, we have a residual $U(1)$ symmetry corresponding to spin rotations around the z axis. Hence, S_z^{tot} is still a good quantum number even in the magnetically ordered states to classify possible coexisting pairing phases. Consequently, the triplet states are additionally split into $S_z^{\text{tot}} = 1$ for $\Delta_l^z(\tau) + \Delta_l^0(\tau)$, $S_z^{\text{tot}} = 0$ for $\Delta_l^x(\tau)$, and $S_z^{\text{tot}} = -1$ for $\Delta_l^0(\tau) - \Delta_l^z(\tau)$.

Since we never encounter p -wave pairing states, or finite S_z^{tot} , in our phase diagram, we will only be focusing on s and d -waves singlet and triplet with $S_z^{\text{tot}} = 0$. We define the action of each of the aforementioned symmetry operations on the electron states, followed by examining how the various order parameters behave under these symmetries.

(i) *Rotation.* $c_{\mathbf{r},1,\alpha} \rightarrow c_{\mathcal{R},\mathbf{r},2,\alpha}$, $c_{\mathbf{r},2,\alpha} \rightarrow c_{\mathcal{R},\mathbf{r},3,\alpha}$, $c_{\mathbf{r},3,\alpha} \rightarrow c_{\mathcal{R},\mathbf{r},4,\alpha}$, $c_{\mathbf{r},4,\alpha} \rightarrow c_{\mathcal{R},\mathbf{r},1,\alpha}$, where \mathcal{R}, \mathbf{r} represents the rotated unit cell position.

(ii) *Time-reversal.* $c_{\mathbf{r},i,\alpha} \rightarrow i\sigma_{\alpha\beta}^y \cdot c_{\mathbf{r},i,\beta}$ followed by a complex conjugation operation \mathcal{K} .

(iii) *Inversion.* $c_{\mathbf{r},1,\alpha} \rightarrow c_{-\mathbf{r},3,\alpha}$, $c_{\mathbf{r},2,\alpha} \rightarrow c_{-\mathbf{r},4,\alpha}$, $c_{\mathbf{r},3,\alpha} \rightarrow c_{-\mathbf{r},1,\alpha}$, $c_{\mathbf{r},4,\alpha} \rightarrow c_{-\mathbf{r},2,\alpha}$.

(iv) *Mirror along x .* $c_{\mathbf{r},1,\alpha} \rightarrow c_{\mathcal{M}_x,\mathbf{r},1,\alpha}$, $c_{\mathbf{r},2,\alpha} \rightarrow c_{\mathcal{M}_x,\mathbf{r},4,\alpha}$, $c_{\mathbf{r},3,\alpha} \rightarrow c_{\mathcal{M}_x,\mathbf{r},3,\alpha}$, $c_{\mathbf{r},4,\alpha} \rightarrow c_{\mathcal{M}_x,\mathbf{r},2,\alpha}$, where $\mathcal{M}_x, \mathbf{r}$ represents the mirrored along x unit-cell position.

(v) *Mirror along y .* $c_{\mathbf{r},1,\alpha} \rightarrow c_{\mathcal{M}_y,\mathbf{r},3,\alpha}$, $c_{\mathbf{r},2,\alpha} \rightarrow c_{\mathcal{M}_y,\mathbf{r},2,\alpha}$, $c_{\mathbf{r},3,\alpha} \rightarrow c_{\mathcal{M}_y,\mathbf{r},1,\alpha}$, $c_{\mathbf{r},4,\alpha} \rightarrow c_{\mathcal{M}_y,\mathbf{r},4,\alpha}$, where $\mathcal{M}_y, \mathbf{r}$ represents the mirrored along y unit-cell position.

We list the corresponding quantum numbers of the pairing states that we are interested in Table I under the aforementioned symmetries.

- [1] D. P. Arovas, E. Berg, S. A. Kivelson, and S. Raghu, The Hubbard model, *Annu. Rev. Condens. Matter Phys.* **13**, 239 (2022).
- [2] E. Dagotto, Correlated electrons in high-temperature superconductors, *Rev. Mod. Phys.* **66**, 763 (1994).

- [3] P. A. Lee, N. Nagaosa, and X.-G. Wen, Doping a Mott insulator: Physics of high-temperature superconductivity, *Rev. Mod. Phys.* **78**, 17 (2006).
- [4] P. W. Anderson, P. A. Lee, M. Randeria, T. M. Rice, N. Trivedi, and F. C. Zhang, The physics behind high-temperature super-

- conducting cuprates: The plain vanilla version of RVB, *J. Phys.: Condens. Matter* **16**, R755 (2004).
- [5] P. Dai, Antiferromagnetic order and spin dynamics in iron-based superconductors, *Rev. Mod. Phys.* **87**, 855 (2015).
 - [6] Q. Si and E. Abrahams, Strong correlations and magnetic frustration in the high T_c iron pnictides, *Phys. Rev. Lett.* **101**, 076401 (2008).
 - [7] J. Dong, H. J. Zhang, G. Xu, Z. Li, G. Li, W. Z. Hu, D. Wu, G. F. Chen, X. Dai, J. L. Luo *et al.*, Competing orders and spin-density-wave instability in $\text{La}(\text{O}_{1-x}\text{F}_x)\text{FeAs}$, *Europhys. Lett.* **83**, 27006 (2008).
 - [8] E. Fawcett, Spin-density-wave antiferromagnetism in chromium, *Rev. Mod. Phys.* **60**, 209 (1988).
 - [9] D. J. Scalapino, Superconductivity and spin fluctuations, [arXiv:cond-mat/9908287](https://arxiv.org/abs/cond-mat/9908287).
 - [10] A. Abanov, A. V. Chubukov, and A. M. Finkel'stein, Coherent vs. incoherent pairing in 2D systems near magnetic instability, *Europhys. Lett.* **54**, 488 (2001).
 - [11] A. V. Chubukov, D. V. Efremov, and I. Eremin, Magnetism, superconductivity, and pairing symmetry in iron-based superconductors, *Phys. Rev. B* **78**, 134512 (2008).
 - [12] A. Chubukov, Pairing mechanism in Fe-based superconductors, *Annu. Rev. Condens. Matter Phys.* **3**, 57 (2012).
 - [13] L. Šmejkal, J. Sinova, and T. Jungwirth, Emerging research landscape of altermagnetism, *Phys. Rev. X* **12**, 040501 (2022).
 - [14] L. Šmejkal, J. Sinova, and T. Jungwirth, Beyond conventional ferromagnetism and antiferromagnetism: A phase with nonrelativistic spin and crystal rotation symmetry, *Phys. Rev. X* **12**, 031042 (2022).
 - [15] S. Bhowal and N. A. Spaldin, Ferroically ordered magnetic octupoles in d -wave altermagnets, *Phys. Rev. X* **14**, 011019 (2024).
 - [16] S. A. Kivelson, I. P. Bindloss, E. Fradkin, V. Oganessian, J. M. Tranquada, A. Kapitulnik, and C. Howald, How to detect fluctuating stripes in the high-temperature superconductors, *Rev. Mod. Phys.* **75**, 1201 (2003).
 - [17] S. Raghu, A. Paramekanti, E. A. Kim, R. A. Borzi, S. A. Grigera, A. P. Mackenzie, and S. A. Kivelson, Microscopic theory of the nematic phase in $\text{Sr}_3\text{Ru}_2\text{O}_7$, *Phys. Rev. B* **79**, 214402 (2009).
 - [18] R. González-Hernández, L. Šmejkal, K. Výborný, Y. Yahagi, J. Sinova, T. c. v. Jungwirth, and J. Železný, Efficient electrical spin splitter based on nonrelativistic collinear antiferromagnetism, *Phys. Rev. Lett.* **126**, 127701 (2021).
 - [19] H. Satoru, Y. Yuki, and K. Hiroaki, Momentum-dependent spin splitting by collinear antiferromagnetic ordering, *J. Phys. Soc. Jpn.* **88**, 123702 (2019).
 - [20] T. Jungwirth, X. Martí, P. Wadley, and J. Wunderlich, Antiferromagnetic spintronics, *Nat. Nanotechnol.* **11**, 231 (2016).
 - [21] J. Sinova, S. O. Valenzuela, J. Wunderlich, C. H. Back, and T. Jungwirth, Spin Hall effects, *Rev. Mod. Phys.* **87**, 1213 (2015).
 - [22] S. Reimers, L. Odenbreit, L. Šmejkal, V. N. Strocov, P. Constantinou, A. B. Hellenes, R. Jaeschke Ubierno, W. H. Campos, V. K. Bharadwaj, A. Chakraborty *et al.*, Direct observation of altermagnetic band splitting in CrSb thin films, *Nat. Commun.* **15**, 2116 (2024).
 - [23] M. Leiviskä, J. Rial, A. Bad'ura, R. L. Seeger, I. Kounta, S. Beckert, D. Kriegner, I. Joumard, E. Schmoranzarová, J. Sinova, O. Gomonay, A. Thomas, S. T. B. Goennenwein, H. Reichlová, L. Šmejkal, L. Michez, T. Jungwirth, and V. Baltz, Anisotropy of the anomalous Hall effect in the altermagnet candidate Mn_5Si_3 , *Phys. Rev. B* **109**, 224430 (2024).
 - [24] T. Osumi, S. Souma, T. Aoyama, K. Yamauchi, A. Honma, K. Nakayama, T. Takahashi, K. Ohgushi, and T. Sato, Observation of a giant band splitting in altermagnetic MnTe, *Phys. Rev. B* **109**, 115102 (2024).
 - [25] Y. Yu, H.-G. Suh, M. Roig, and D. F. Agterberg, Altermagnetism from coincident van Hove singularities: Application to $\kappa\text{-Cl}$, [arXiv:2402.05180](https://arxiv.org/abs/2402.05180).
 - [26] P. A. McClarty and J. G. Rau, Landau theory of altermagnetism, *Phys. Rev. Lett.* **132**, 176702 (2024).
 - [27] H. Schiff, A. Corticelli, A. Guerreiro, J. Romhányi, and P. McClarty, The spin point groups and their representations, [arXiv:2307.12784](https://arxiv.org/abs/2307.12784).
 - [28] D. S. Antonenko, R. M. Fernandes, and J. W. F. Venderbos, Mirror Chern bands and Weyl nodal loops in altermagnets, [arXiv:2402.10201](https://arxiv.org/abs/2402.10201).
 - [29] R. M. Fernandes, V. S. de Carvalho, T. Birol, and R. G. Pereira, Topological transition from nodal to nodeless Zeeman splitting in altermagnets, *Phys. Rev. B* **109**, 024404 (2024).
 - [30] C. R. W. Steward, R. M. Fernandes, and J. Schmalian, Dynamic paramagnon-polarons in altermagnets, *Phys. Rev. B* **108**, 144418 (2023).
 - [31] B. Brekke, A. Brataas, and A. Sudbø, Two-dimensional altermagnets: Superconductivity in a minimal microscopic model, *Phys. Rev. B* **108**, 224421 (2023).
 - [32] H. G. Gill, B. Brekke, J. Linder, and A. Brataas, Quasiclassical theory of superconducting spin-splitter effects and spin-filtering via altermagnets, *Phys. Rev. B* **110**, L140506 (2024).
 - [33] S.-B. Zhang, L.-H. Hu, and T. Neupert, Finite-momentum Cooper pairing in proximitized altermagnets, *Nat. Commun.* **15**, 1801 (2024).
 - [34] K. Maeland, B. Brekke, and A. Sudbø, Many-body effects on superconductivity mediated by double-magnon processes in altermagnets, *Phys. Rev. B* **109**, 134515 (2024).
 - [35] R. Soto-Garrido and E. Fradkin, Pair-density-wave superconducting states and electronic liquid-crystal phases, *Phys. Rev. B* **89**, 165126 (2014).
 - [36] D. Zhu, Z.-Y. Zhuang, Z. Wu, and Z. Yan, Topological superconductivity in two-dimensional altermagnetic metals, *Phys. Rev. B* **108**, 184505 (2023).
 - [37] K. Flensberg, F. von Oppen, and A. Stern, Engineered platforms for topological superconductivity and Majorana zero modes, *Nat. Rev. Mater.* **6**, 944 (2021).
 - [38] S. A. A. Ghorashi, T. L. Hughes, and J. Cano, Altermagnetic routes to Majorana modes in zero net magnetization, *Phys. Rev. Lett.* **133**, 106601 (2024).
 - [39] J. A. Ouassou, A. Brataas, and J. Linder, dc Josephson effect in altermagnets, *Phys. Rev. Lett.* **131**, 076003 (2023).
 - [40] S. Banerjee and M. S. Scheurer, Altermagnetic superconducting diode effect, *Phys. Rev. B* **110**, 024503 (2024).
 - [41] V. J. Emery, Theory of high- T_c superconductivity in oxides, *Phys. Rev. Lett.* **58**, 2794 (1987).
 - [42] V. J. Emery and G. Reiter, Mechanism for high-temperature superconductivity, *Phys. Rev. B* **38**, 4547 (1988).
 - [43] C. M. Varma, Non-fermi-liquid states and pairing instability of a general model of copper oxide metals, *Phys. Rev. B* **55**, 14554 (1997).

- [44] M. H. Fischer, S. Wu, M. Lawler, A. Paramakanti, and E.-A. Kim, Nematic and spin-charge orders driven by hole-doping a charge-transfer insulator, *New J. Phys.* **16**, 093057 (2014).
- [45] H. Watanabe, T. Shirakawa, K. Seki, H. Sakakibara, T. Kotani, H. Ikeda, and S. Yunoki, Unified description of cuprate superconductors using a four-band $d-p$ model, *Phys. Rev. Res.* **3**, 033157 (2021).
- [46] P. Mai, G. Balduzzi, S. Johnston, and T. A. Maier, Orbital structure of the effective pairing interaction in the high-temperature superconducting cuprates, *npj Quantum Mater.* **6**, 26 (2021).
- [47] H. Miyahara, R. Arita, and H. Ikeda, Development of a two-particle self-consistent method for multiorbital systems and its application to unconventional superconductors, *Phys. Rev. B* **87**, 045113 (2013).
- [48] O. Gingras, N. Allaglo, R. Nourafkan, M. Côté, and A.-M. S. Tremblay, Superconductivity in correlated multiorbital systems with spin-orbit coupling: Coexistence of even- and odd-frequency pairing, and the case of Sr_2RuO_4 , *Phys. Rev. B* **106**, 064513 (2022).
- [49] A. C. Yuan, E. Berg, and S. A. Kivelson, Multiband mean-field theory of the $d + ig$ superconductivity scenario in Sr_2RuO_4 , *Phys. Rev. B* **108**, 014502 (2023).
- [50] C.-Y. Moon, Effects of orbital selective dynamical correlation on the spin susceptibility and superconducting symmetries in Sr_2RuO_4 , *Phys. Rev. Res.* **5**, L022058 (2023).
- [51] H. Suzuki, L. Wang, J. Bertinshaw, H. U. R. Strand, S. Käser, M. Krautloher, Z. Yang, N. Wentzell, O. Parcollet, F. Jerzembeck *et al.*, Distinct spin and orbital dynamics in Sr_2RuO_4 , *Nat. Commun.* **14**, 7042 (2023).
- [52] Q. Si, R. Yu, and E. Abrahams, High-temperature superconductivity in iron pnictides and chalcogenides, *Nat. Rev. Mater.* **1**, 16017 (2016).
- [53] D. Li, K. Lee, B. Y. Wang, M. Osada, S. Crossley, H. R. Lee, Y. Cui, Y. Hikita, and H. Y. Hwang, Superconductivity in an infinite-layer nickelate, *Nature (London)* **572**, 624 (2019).
- [54] H. Sun, M. Huo, X. Hu, J. Li, Z. Liu, Y. Han, L. Tang, Z. Mao, P. Yang, B. Wang *et al.*, Signatures of superconductivity near 80 K in a nickelate under high pressure, *Nature (London)* **621**, 493 (2023).
- [55] H. Sakakibara, H. Usui, K. Suzuki, T. Kotani, H. Aoki, and K. Kuroki, Model construction and a possibility of cupratelike pairing in a new d^9 nickelate superconductor (Nd, Sr) NiO_2 , *Phys. Rev. Lett.* **125**, 077003 (2020).
- [56] L.-H. Hu and C. Wu, Two-band model for magnetism and superconductivity in nickelates, *Phys. Rev. Res.* **1**, 032046(R) (2019).
- [57] P. Adhikary, S. Bandyopadhyay, T. Das, I. Dasgupta, and T. Saha-Dasgupta, Orbital-selective superconductivity in a two-band model of infinite-layer nickelates, *Phys. Rev. B* **102**, 100501(R) (2020).
- [58] X. Wu, D. Di Sante, T. Schwemmer, W. Hanke, H. Y. Hwang, S. Raghu, and R. Thomale, Robust $d_{x^2-y^2}$ -wave superconductivity of infinite-layer nickelates, *Phys. Rev. B* **101**, 060504(R) (2020).
- [59] Z. Wang, G.-M. Zhang, Y.-f. Yang, and F.-C. Zhang, Distinct pairing symmetries of superconductivity in infinite-layer nickelates, *Phys. Rev. B* **102**, 220501(R) (2020).
- [60] P. Werner and S. Hoshino, Nickelate superconductors: Multi-orbital nature and spin freezing, *Phys. Rev. B* **101**, 041104(R) (2020).
- [61] Y.-H. Zhang and A. Vishwanath, Type-II $t-J$ model in superconducting nickelate $\text{Nd}_{1-x}\text{Sr}_x\text{NiO}_2$, *Phys. Rev. Res.* **2**, 023112 (2020).
- [62] S.-H. Baek, D. V. Efremov, J. M. Ok, J. S. Kim, J. van den Brink, and B. Büchner, Orbital-driven nematicity in FeSe , *Nat. Mater.* **14**, 210 (2015).
- [63] J. K. Glasbrenner, I. I. Mazin, H. O. Jeschke, P. J. Hirschfeld, R. M. Fernandes, and R. Valenti, Effect of magnetic frustration on nematicity and superconductivity in iron chalcogenides, *Nat. Phys.* **11**, 953 (2015).
- [64] Q. Wang, Y. Shen, B. Pan, Y. Hao, M. Ma, F. Zhou, P. Steffens, K. Schmalzl, T. R. Forrest, M. Abdel-Hafiez *et al.*, Strong interplay between stripe spin fluctuations, nematicity and superconductivity in FeSe , *Nat. Mater.* **15**, 159 (2016).
- [65] D. F. Agterberg, J. C. S. Davis, S. D. Edkins, E. Fradkin, D. J. Van Harlingen, S. A. Kivelson, P. A. Lee, L. Radzihovsky, J. M. Tranquada, and Y. Wang, The physics of pair-density waves: Cuprate superconductors and beyond, *Annu. Rev. Condens. Matter Phys.* **11**, 231 (2020).
- [66] P. Nikolić, A. A. Burkov, and A. Paramakanti, Finite momentum pairing instability of band insulators with multiple bands, *Phys. Rev. B* **81**, 012504 (2010).
- [67] H.-C. Jiang and T. P. Devereaux, Pair density wave and superconductivity in a kinetically frustrated doped Emery model on a square lattice, *Frontiers in Electronic Materials* **3** (2023).
- [68] Y.-M. Wu, P. A. Nosov, A. A. Patel, and S. Raghu, Pair density wave order from electron repulsion, *Phys. Rev. Lett.* **130**, 026001 (2023).
- [69] C. Setty, L. Fanfarillo, and P. J. Hirschfeld, Mechanism for fluctuating pair density wave, *Nat. Commun.* **14**, 3181 (2023).
- [70] N. S. Ticea, S. Raghu, and Y.-M. Wu, Pair density wave order in multiband systems, *Phys. Rev. B* **110**, 094515 (2024).
- [71] Y.-T. Kang, C. Lu, F. Yang, and D.-X. Yao, Single-orbital realization of high-temperature s^\pm superconductivity in the square-octagon lattice, *Phys. Rev. B* **99**, 184506 (2019).
- [72] L. H. C. M. Nunes and C. M. Smith, Flat-band superconductivity for tight-binding electrons on a square-octagon lattice, *Phys. Rev. B* **101**, 224514 (2020).
- [73] P. Wunderlich, F. Ferrari, and R. Valentí, Detecting topological phases in the square-octagon lattice with statistical methods, *Europhys. J. Plus* **138**, 336 (2023).
- [74] S. M. Nie, Z. Song, H. Weng, and Z. Fang, Quantum spin Hall effect in two-dimensional transition-metal dichalcogenide haeckelites, *Phys. Rev. B* **91**, 235434 (2015).
- [75] Y. Zhang, J. Lee, W.-L. Wang, and D.-X. Yao, Two-dimensional octagon-structure monolayer of nitrogen group elements and the related nano-structures, *Comput. Mater. Sci.* **110**, 109 (2015).
- [76] F. C. Zhang, C. Gros, T. M. Rice, and H. Shiba, A renormalised Hamiltonian approach to a resonant valence bond wavefunction, *Supercond. Sci. Technol.* **1**, 36 (1988).
- [77] J. D. Sau and S. Sachdev, Mean-field theory of competing orders in metals with antiferromagnetic exchange interactions, *Phys. Rev. B* **89**, 075129 (2014).

- [78] V. Leeb, A. Mook, L. Šmejkal, and J. Knolle, Spontaneous formation of altermagnetism from orbital ordering, *Phys. Rev. Lett.* **132**, 236701 (2024).
- [79] P. Das, V. Leeb, J. Knolle, and M. Knap, Realizing altermagnetism in Fermi-Hubbard models with ultracold atoms, *Phys. Rev. Lett.* **132**, 263402 (2024).
- [80] [TightBindingToolkit.jl](#).
- [81] [MeanFieldToolkit.jl](#).
- [82] O. Parcollet, M. Ferrero, T. Ayrat, H. Hafermann, I. Krivenko, L. Messio, and P. Seth, TRIQS: A toolbox for research on interacting quantum systems, *Comput. Phys. Commun.* **196**, 398 (2015).